

Radiative corrections to the direct detection of the Higgsino-(and Wino-)like neutralino dark matter: Spin-dependent interactions

Subhadip Bisal,^{1,2,*} Arindam Chatterjee,^{3,†} Debottam Das,^{1,2,‡} and Syed Adil Pasha^{3,§}

¹*Institute of Physics, Sachivalaya Marg, Bhubaneswar, 751 005, India*

²*Homi Bhabha National Institute, Training School Complex, Anushakti Nagar, Mumbai 400 094, India*

³*Shiv Nadar Institution of Eminence deemed to be University,
Gautam Buddha Nagar, Uttar Pradesh, 201314, India*

The lightest neutralino ($\tilde{\chi}_1^0$) is a promising dark matter (DM) candidate in the R-parity conserving minimal supersymmetric standard model (MSSM). In this work, we focus on dominantly Higgsino-like and Wino-like $\tilde{\chi}_1^0$ DM, with small admixtures of gauginos and Higgsinos, respectively. In particular, we explore large one-loop corrections to the $\tilde{\chi}_1^0\tilde{\chi}_1^0Z$ vertex, which can significantly affect the estimation of the spin-dependent $\tilde{\chi}_1^0$ -nucleon scattering cross-section in the regions where such DM candidates are viable. We have used the on-shell renormalization scheme to estimate the relevant counterterm contributions. In the parameter region where $\tilde{\chi}_1^0$ is dominantly Higgsino-like, the radiative corrections (including the contributions from the respective counterterms) are substantial and can enhance the $\tilde{\chi}_1^0\tilde{\chi}_1^0Z$ vertex by up to $\sim 120\%$ for the benchmark scenarios we have considered. Further, for an almost pure Wino-like $\tilde{\chi}_1^0$, the increment in the $\tilde{\chi}_1^0\tilde{\chi}_1^0Z$ vertex is up to 15%. The corresponding cross-sections with the proton and the neutron can be changed by up to about 50%. In addition, including the electroweak box diagrams, the cross-sections can be significantly enhanced, in particular, for the Wino-like $\tilde{\chi}_1^0$.

I. INTRODUCTION

There has been ample evidence of existence of non-luminous matter, i.e., dark matter (DM), in our Universe [1–3]. Cosmological observations suggest that DM constitutes about 26% of the energy budget of the Universe [4, 5]. In the standard model of particle physics (SM) there is no suitable candidate for DM. However, several well-motivated extensions of SM incorporates suitable DM candidates [1, 6].

Among the theoretical frameworks for beyond SM, supersymmetric extensions have been well studied. In particular, the minimal supersymmetric standard model (MSSM) with conserved R -parity has been widely

* subhadip.b@iopb.res.in

† arindam.chatterjee@snu.edu.in

‡ debottam@iopb.res.in

§ sp855@snu.edu.in

studied in the literature. In this scenario, in the parameter regions where the lightest neutralino ($\tilde{\chi}_1^0$) is the lightest odd particle under R -parity, the particle remains stable, and is a suitable candidate for DM. One of the prime motivations of the supersymmetric theories have been addressing the naturalness concerns [7–13]. Stringent limits from the large hadron collider (LHC) on the masses of the heavy supersymmetric partners [14–20] have been in tension with naturalness requirements [12, 13, 21–23]. To quantify the naturalness, several measures of fine-tuning have been proposed in the literature, and such measures involve the Higgsino mass parameter μ . One such measure, which uses the relevant parameters at the electroweak scale, suggests that a rather small Higgsino mass parameter μ (of $\mathcal{O}(100)$ GeV), is essential for electroweak naturalness.¹ In its minimal incarnation, assuming the gaugino mass parameters are very large $|\mu| \ll |M_1|, M_2$, a small μ parameter leads to Higgsino-like neutralino as the lightest stable particle (LSP).

There have been numerous studies on the search of compressed neutralino spectra, including for Higgsino-like neutralinos at the LHC as well as in the direct and indirect DM detection experiments. The limits from the LHC on the compressed Higgsino spectrum, as mentioned above, is rather weak. Complimentary constraints on the μ parameter can be obtained with Higgsino-like neutralinos as DM candidates [24–27], from the direct [28–31] and indirect [32–34] searches for DM.²

The prospects of direct detection of such neutralino DM critically depend on the composition of the $\tilde{\chi}_1^0$. For a pure Higgsino-like $\tilde{\chi}_1^0$, the tree-level interaction strength with the Higgs bosons, as well as with Z boson, which dictate the spin-independent and spin-dependent $\tilde{\chi}_1^0$ -nucleon cross-sections respectively, remain suppressed. Thus the radiative corrections to the respective vertices play an important role in determining the prospects of the direct detection. The importance of the radiative corrections in the context of the spin-independent as well as the spin-dependent direct searches have been studied in the literature in Refs.[36–41].³ In this article, we focus on some dominant radiative corrections which contribute to the spin-dependent direct detection cross-sections of the Higgsino-like DM. In particular, we evaluate the corrections to the $\tilde{\chi}_1^0\tilde{\chi}_1^0Z$ vertex, which affects the spin-dependent $\tilde{\chi}_1^0$ -nucleon cross-section. Suitable versions of the on-shell renormalization scheme [50–52] have been used to renormalize the chargino-neutralino sector and contributions from the relevant vertex counterterms have been computed. In this context, we recall that, in Ref.[36] some dominant contributions to the $\tilde{\chi}_1^0\tilde{\chi}_1^0Z$ vertex corrections from the loops involving the 3rd generation quark-squarks have been considered and results were presented for rather light Higgsino-like states, approximately accounting for the effect of the gaugino-Higgsino mixing. The

¹ Following the “electroweak” naturalness criteria, the fine-tuning measure has been estimated to be about $\mathcal{O}(10 - 100)$ assuming the masses of the third generation squarks and gluons in the ballpark of several TeV [12].

² Even for a Bino-dominated LSP accompanied with a Higgsino component, indirect searches may become important in particular context [35].

³ Some important radiative corrections to the direct detection process and the relic abundance in the context of neutralino DM have been studied in Refs.[42–49].

contributions from the loops involving the other (s)particles have not been considered. Additionally, in Refs.[37–39] important radiative corrections to the $\tilde{\chi}_1^0\tilde{\chi}_1^0Z$ vertex involving the electroweak gauge bosons, as well as contributions from the electroweak box diagrams have been considered for Higgsino-like and Wino-like neutralino dark matter in the limit of respective pure gauge eigenstates. However, the sfermions and fermions were assumed to be heavy and thus, their contributions have been ignored. The present work takes into account the loop contributions from all the sfermions and fermions, as well as, gauge bosons, Higgs bosons and chargino-neutralinos respecting the relevant experimental constraints. Further, as mentioned, full vertex renormalization, including contributions from the vertex counterterms in the on-shell renormalization scheme, have been taken into account. The radiative corrections are then used to estimate the spin-dependent cross-section. This is performed by implementing these corrections in the publicly available package `micrOMEGAs` [53, 54]. Further, significant contributions from the electroweak box diagrams to the spin-dependent $\tilde{\chi}_1^0$ -nucleon scattering have been incorporated following Refs.[37–39]. While the main focus of this work is on Higgsino-like $\tilde{\chi}_1^0$, a similar study on the Wino-like $\tilde{\chi}_1^0$ have also been pursued in this context of spin-dependent interactions. In case of Wino-like $\tilde{\chi}_1^0$, radiative corrections to the $\tilde{\chi}_1^0\tilde{\chi}_1^0Z$ vertex from loops involving gauge bosons, neutralinos and charginos, and from the (s)fermions have been considered. As before, the vertex counterterms have been estimated using the on-shell renormalization scheme. Finally, dominant contributions from the electroweak box diagrams have been included following Refs.[38, 55]. As in the previous case, the radiative corrections are then implemented in the publicly available package `micrOMEGAs` [53, 54] and their effect on the spin-dependent interactions have been discussed.⁴

The thermal relic density of $\Omega_{\text{DM}}h^2 \approx 0.12$ in the early universe is achieved for a Higgsino-like $\tilde{\chi}_1^0$ with the Higgsino mass parameter μ around 1 TeV, and for a Wino-like $\tilde{\chi}_1^0$ mass parameter M_2 of about 2 TeV⁵, the details also depend on the other supersymmetric sparticle spectra.⁶ Note that in case of $\tilde{\chi}_1^0$ constituting only a fraction of the DM content of the universe, the direct detection bounds are relaxed in the same proportion. In this article, we will not concern ourselves with satisfying the thermal relic abundance of the early universe.

This article is organized as follows. In section II, we present the theoretical outline of the chargino-neutralino sector and the tree-level coupling of the neutralino with the Z boson. In section IIB, we

⁴ It is worth noting that, the Wino mass parameter M_2 can be smaller than $|\mu|, |M_1|$ in specific realizations of the high scale models, in particular, where anomaly mediated supersymmetry breaking (AMSB) may be realized [56, 57]. Thus, in such scenarios, $\tilde{\chi}_1^0$ can be Wino-like.

⁵ Considering Sommerfeld enhancement leads to an enhanced (co-)annihilation cross-section for rather heavy ($\mathcal{O}(1\text{TeV})$) neutralino DM [58–62]. For the Wino-like $\tilde{\chi}_1^0$ the correct relic density is achieved at $M_2 \sim 2.7 - 3$ TeV.

⁶ These mass scales can be brought down if we consider coannihilation effects, see, e.g. [63]. Moreover, there are scenarios discussed in literature for non-thermal production of DM [64]. Further, there may exist other components of dark matter, i.e., axions, etc. which may resolve the under-abundance of lower mass Higgsino or Wino-like $\tilde{\chi}_1^0$ DM [65].

motivate the Higgsino-like and Wino-like LSP and their direct detection via underground and ground based detectors. Section III contains the results of our work for both Higgsino-like as well as Wino-like case and their discussion. In section IV, we conclude our work.

II. THE FRAMEWORK

In this section, we begin by discussing the chargino-neutralino sector in the MSSM; see, e.g., [66], for a review. In particular, we focus on the parameter region with a Higgsino-like and a Wino-like lightest neutralino. Subsequently, we discuss the generalities of spin-dependent $\tilde{\chi}_1^0$ -nucleus scattering, and emphasize the implications of radiative corrections to the $\tilde{\chi}_1^0\tilde{\chi}_1^0Z$ vertex on the respective cross-section.

A. The Chargino-Neutralino Spectrum

The tree-level mass Lagrangian for the charginos can be expressed in the gauge eigenbasis in terms of the Weyl spinors (the charged Winos \widetilde{W}^+ and \widetilde{W}^- , and the Higgsinos \tilde{h}_i^\pm for $i \in \{1, 2\}$) with $\psi^+ = (\widetilde{W}^+, \tilde{h}_2^+)$ and $\psi^- = (\widetilde{W}^-, \tilde{h}_1^-)$, as [66]:

$$-\mathcal{L}_{\text{Mass}}^c = \psi^{-T} M^c \psi^+ + H.C. \quad (1)$$

here M^c is the mass matrix written as:

$$M^c = \begin{pmatrix} M_2 & \sqrt{2}M_W \sin \beta \\ \sqrt{2}M_W \cos \beta & \mu \end{pmatrix}. \quad (2)$$

In the above expression, M_2 and μ represent the supersymmetry-breaking $SU(2)$ Wino mass parameter and the supersymmetric Higgsino mass parameter, respectively; M_W denotes the mass of the W boson, and $\tan \beta$ is the ratio of the vacuum expectation values (*vevs*) of the up-type and down-type CP-even neutral Higgs bosons. The chargino mass matrix M^c can be diagonalized through a bi-unitary transformation with the help of unitary matrices U and V to get:

$$M_D^c = U^* M^c V^{-1} = \text{Diagonal}(m_{\tilde{\chi}_1^+}, m_{\tilde{\chi}_2^+}), \quad (3)$$

The mass eigenstates are ordered as: $m_{\tilde{\chi}_1^+} \leq m_{\tilde{\chi}_2^+}$. For the charginos ($\tilde{\chi}_i^+$ with $i \in \{1, 2\}$), the left-handed and right-handed components of these mass eigenstates can be expressed as:

$$\mathbf{P}_L \tilde{\chi}_i^+ = V_{ij} \psi_j^+, \quad \mathbf{P}_R \tilde{\chi}_i^+ = U_{ij}^* \overline{\psi_j^-}, \quad (4)$$

where \mathbf{P}_L and \mathbf{P}_R are the standard projection operators, $\overline{\psi_j^-} = \psi_j^{-\dagger}$, and j is summed over.

The neutralino states consists of the Bino (\tilde{B}^0), the neutral Wino (\tilde{W}^3), and the down-type and up-type neutral Higgsinos (\tilde{h}_1^0 and \tilde{h}_2^0 , respectively). Written in the gauge eigenbasis, $\psi^0 = (\tilde{B}, \tilde{W}^3, \tilde{h}_1^0, \tilde{h}_2^0)$, the Lagrangian for the mass term assumes the form [66]:

$$-\mathcal{L}_{\text{Mass}}^n = \frac{1}{2} \psi^{0T} M^n \psi^0 + \text{h.c.} \quad (5)$$

M^n is the neutralino mass matrix given by,

$$M^n = \begin{pmatrix} M_1 & 0 & -M_Z s_W c_\beta & M_Z s_W s_\beta \\ 0 & M_2 & M_Z c_W c_\beta & -M_Z c_W s_\beta \\ -M_Z s_W c_\beta & M_Z c_W c_\beta & 0 & -\mu \\ M_Z s_W s_\beta & -M_Z c_W s_\beta & -\mu & 0 \end{pmatrix}. \quad (6)$$

In Eqs.(3) and (6), s_W , s_β , c_W , and c_β represent $\sin \theta_W$, $\sin \beta$, $\cos \theta_W$, and $\cos \beta$ respectively, where θ_W is the weak mixing angle. M_Z denotes the mass of the Z boson, and M_1 is the supersymmetry breaking $U(1)_Y$ gaugino (Bino) mass parameter. In order to determine the masses of the neutralinos, the matrix M^n can be diagonalized by a unitary matrix N as follows:

$$M_D^n = N^* M^n N^{-1} = \text{Diagonal}(m_{\tilde{\chi}_1^0}, m_{\tilde{\chi}_2^0}, m_{\tilde{\chi}_3^0}, m_{\tilde{\chi}_4^0}) \quad (7)$$

The mass eigenstates ($\tilde{\chi}_i^0$) are arranged in increasing order of their corresponding mass eigenvalues: $m_{\tilde{\chi}_1^0} \leq m_{\tilde{\chi}_2^0} \leq m_{\tilde{\chi}_3^0} \leq m_{\tilde{\chi}_4^0}$ (in absolute value). These eigenstates are charge conjugates of themselves, i.e., $\tilde{\chi}_i^{0C} = \tilde{\chi}_i^0$, where the superscript C denotes charge conjugation. For the Majorana neutralinos $\tilde{\chi}_i^0$ ($i \in \{1, 2, 3, 4\}$), the left-handed components of these mass eigenstates can be expressed as:

$$\mathbf{P}_L \tilde{\chi}_i^0 = N_{ij} \psi_j^0, \quad (8)$$

where j is summed over again and N_{ij} refers to the $\{i, j\}^{\text{th}}$ element of the matrix N in Eq.(7).

Analytical expressions for the mass eigenvalues of charginos and neutralinos are available in the literature [1, 67–69]. But, we can numerically estimate these eigenvalues (esp. for neutralinos) in a straightforward and practical manner.

In the present context, we state the approximate mass eigenvalues for the Higgsino-like and the Wino-like neutralinos, in the limit of negligible mixing. In the parameter region where the Higgsino mass parameter is notably smaller compared to the gaugino mass parameters, i.e., $|\mu| \ll |M_1|, M_2$, the masses of the light Higgsino-like particles can be approximated as [36, 70]:

$$\begin{aligned} m_{\tilde{\chi}_1^\pm} &= |\mu| \left(1 - \frac{M_W^2 \sin 2\beta}{\mu M_2} \right) + \mathcal{O}(M_2^{-2}) + \text{rad.corr.} \\ m_{\tilde{\chi}_{a,s}^0} &= \pm \mu - \frac{M_Z^2}{2} (1 \pm \sin 2\beta) \left(\frac{s_W^2}{M_1} + \frac{c_W^2}{M_2} \right) + \text{rad.corr.} \end{aligned} \quad (9)$$

In the expression above, subscripts $a(s)$ denote anti-symmetric (symmetric) combinations of up-type (\tilde{h}_2^0) and down-type (\tilde{h}_1^0) Higgsinos constituting the respective mass eigenstates. The symmetric and anti-symmetric states refer to Higgsino-like states composed without and with a relative sign between N_{i3} and N_{i4} , respectively.⁷

In the parameter region where the Wino mass parameter is much smaller compared to the Bino and Higgsino mass parameters, i.e., $M_2 \ll |M_1|, |\mu|$, the masses of the Wino-like states can be approximated as follows [37],

$$\begin{aligned} m_{\tilde{\chi}_1^\pm} &= M_2 + \frac{M_W^2}{M_2^2 - \mu^2} (M_2 + \mu \sin 2\beta) + \text{rad.corr.} + \dots \\ m_{\tilde{\chi}_1^0} &= M_2 + \frac{M_W^2}{M_2^2 - \mu^2} (M_2 + \mu \sin 2\beta) + \text{rad.corr.} + \dots \end{aligned} \quad (10)$$

Although at the tree-level the mass difference Δm_1 is very small, it has been noted that sizable mass splitting of $\mathcal{O}(100)$ MeV can be achieved via the radiative corrections in the limit of negligible Higgsino-gaugino mixing. Thus, as stated in the previous case, in the next section we only focus on the the elastic scattering of $\tilde{\chi}_1^0$ with nucleons which will be relevant in direct detection experiments.

B. Dark Matter direct detection : spin-dependent interactions between $\tilde{\chi}_1^0$ and nucleus

1. Generalities of spin-dependent interactions

We briefly review the generalities of the spin-dependent DM-nucleon interactions in the context of $\tilde{\chi}_1^0$ DM following Refs.[6, 75–77]. The effective Lagrangian for the $\tilde{\chi}_1^0$ -nucleon spin-dependent interaction is given by [6, 75, 76, 78],

$$\mathcal{L}_{\text{eff}} \supset g_N \bar{\chi} \gamma_\mu \gamma_5 \chi \bar{\psi}_N \gamma^\mu \gamma_5 \psi_N, \quad (11)$$

where g_N is the effective coupling, $N \in \{n, p\}$ denotes a neutron or a proton and ψ_N denotes the respective quantum field. At the parton level, the relevant effective Lagrangian describing the $\tilde{\chi}_1^0$ -quark interactions is given by [6, 75–78],

$$\mathcal{L}_{\text{eff,SD}}^q \supset d_q \bar{\tilde{\chi}}_1^0 \gamma^\mu \gamma_5 \tilde{\chi}_1^0 \bar{\psi}_q \gamma_\mu \gamma_5 \psi_q, \quad (12)$$

⁷ It has been noted in the literature that, due to mixing effects, the mass differences $\Delta m_1 = m_{\tilde{\chi}_1^\pm} - m_{\tilde{\chi}_1^0}$ may become very small in certain regions of the parameter space [71–74]. In this context, we focus on mass differences $\Delta m_1, \Delta m_2 \gg \mathcal{O}(1 \text{ MeV})$, where $\Delta m_2 = m_{\tilde{\chi}_2^0} - m_{\tilde{\chi}_1^0}$. Therefore, as discussed in the next section, only the elastic scattering of $\tilde{\chi}_1^0$ with nucleons will be relevant in direct detection experiments.

where q denotes the (light) quark under consideration, ψ_q denotes the respective quantum field and d_q denotes the respective effective coupling. g_N can be expressed in terms of the effective interaction strength d_q as follows [6, 75, 76],

$$g_N = \sum_{q=u,d,s} d_q \Delta q_N. \quad (13)$$

In the above expression Δq_N , which is a measure of the fraction of spin of nucleon N contributed by the constituent quark q , is related to the matrix element of the respective quark axial-vector current, which is given by,

$$\langle N | \bar{\psi}_q \gamma^\mu \gamma_5 \psi_q | N \rangle = 2s_N^\mu \Delta q_N. \quad (14)$$

In the above equation, d_q denotes the parton level effective coupling involving axial vector currents of quarks and $\tilde{\chi}_1^0$. Further, s_N^μ denotes the spin of the nucleon N . Δq^N are extracted from experimental data, see, e.g., Ref.[79].⁸

Note that, for the nucleon at rest, the $\mu = 0$ component of the axial-vector current vanishes. To obtain the spin-dependent $\tilde{\chi}_1^0$ -nucleus scattering cross-section, next, the matrix element of the nucleon spin operators in the nuclear state is estimated. At zero momentum transfer, it is given by the expectation value of the spin content of the protons and neutrons in the nucleus \tilde{N} , denoted by $\langle S_p \rangle = \langle \tilde{N} | S_p | \tilde{N} \rangle$ and $\langle S_n \rangle = \langle \tilde{N} | S_n | \tilde{N} \rangle$ respectively [6, 80]. Further, a suitable form factor $S(k)$ (where $k = |\vec{k}|$ gives the magnitude of the momentum transfer) is introduced to account for non-zero momentum transfer. In terms of the isoscalar and the isovector parameters $a_0 = (\sqrt{2}G_F)^{-1}(g_p + g_n)$ and $a_1 = (\sqrt{2}G_F)^{-1}(g_p - g_n)$, where $G_F = \frac{g_2^2}{8m_W^2}$, m_W denotes the mass of W boson and the subscripts p , n denote proton and neutron respectively. The form factor $S(k)$, then can be expressed as,

$$S(k) = a_0^2 S_{00}(k) + a_1^2 S_{11}(k) + a_0 a_1 S_{01}(k), \quad (15)$$

where, the interference of the isoscalar and the isovector terms give rise to three independent form factors S_{ij} , $i, j \in \{0, 1\}$ [6, 80].⁹ Finally, in the limit of zero momentum transfer, the spin-dependent $\tilde{\chi}_1^0$ - nucleus differential scattering cross-section ($\sigma_0^{\tilde{N}}_{\text{SD}}$) can be expressed as [6, 80, 83]

$$\frac{d\sigma_0^{\tilde{N}}_{\text{SD}}}{dk^2} = \frac{4}{\pi v^2} (g_p \langle S_p \rangle + g_n \langle S_n \rangle)^2 \frac{(J+1)}{J}. \quad (16)$$

⁸ We follow the publicly available package `micrOMEGAs` in this regard, which adopted these from Ref.[79]. Further details in this regard can be found in Appendix A.

⁹ We follow the form factors implemented in the publicly available code `micrOMEGAs` [81]. For the present work, see also Refs.[6, 80, 82].

In the above expression, v denotes the relative speed of the DM with respect to the target nucleus and J denotes the total angular momentum of the nucleus. The effect of non-zero momentum transfer, as usual, is captured by introducing a suitable form factor $\mathcal{F}^2(k) = \frac{S(k)}{S(0)}$, as discussed above. The respective differential cross-section is given by [6],

$$\frac{d\sigma_{\text{SD}}^{\tilde{N}}}{dk^2} = \frac{d\sigma_{0\text{SD}}^{\tilde{N}}}{dk^2} \frac{S(k)}{S(0)}. \quad (17)$$

The total spin-dependent scattering cross-section, in the limit of zero momentum transfer is given by [6],

$$\sigma_{0\text{SD}}^{\tilde{N}} = 4m_r^2 v^2 \frac{d\sigma_{0\text{SD}}^{\tilde{N}}}{dk^2} = \frac{16}{\pi} m_r^2 \frac{(J+1)}{J} (g_p \langle S_p \rangle + g_n \langle S_n \rangle)^2 \quad (18)$$

where, $m_r = \frac{m_{\tilde{\chi}_1^0} m_T}{m_{\tilde{\chi}_1^0} + m_T}$ denotes the reduced mass of the target nucleus (\tilde{N}) (with mass m_T) and $\tilde{\chi}_1^0$. In the following subsection, we discuss the relevant $\tilde{\chi}_1^0$ -quark effective interaction within the framework of MSSM.

2. Spin-dependent interaction at tree-level and at one loop : the case for Higgsino-like and Wino-like $\tilde{\chi}_1^0$ DM

As stated in the Introduction, in the present context we focus on the spin-dependent interactions between $\tilde{\chi}_1^0$ and nucleus. In particular, Higgsino-like and Wino-like $\tilde{\chi}_1^0$ states are of interest. The relevant effective Lagrangian describing the spin-dependent $\tilde{\chi}_1^0$ -nucleon interaction has been described already in Eq.(11).

At the level of partons, the tree-level contributions to the $\tilde{\chi}_1^0$ -quark scattering comes from the Z -boson exchange (t -channel) process, as well as from the respective squark exchange (s -channel) processes [6, 75–78]. At the tree-level, the effective coupling d_q , as described in Eq.(12), receives contributions from the processes mentioned above. These contributions can be described as [77]

$$d_q^{\text{tree}} = \frac{1}{4} \sum_{i=1}^2 \frac{a_{\tilde{q}_i}^2 + b_{\tilde{q}_i}^2}{m_{\tilde{q}_i}^2 - (m_q + m_{\tilde{\chi}_1^0})^2} - \frac{g_2^2}{4c_W^2 M_Z^2} \mathcal{N}_{11}^R T_{3q} \quad (19)$$

where q denotes the light quarks (u,d,s) with mass m_q , T_{3q} is the respective weak isospin, g_2 denotes the $SU(2)_L$ gauge coupling and \mathcal{N}_{11}^R denotes the coupling of neutralinos with Z boson, which will be described below. The first term involves a sum over the two squark mass eigenstates \tilde{q}_i , $i \in \{1, 2\}$ of the same flavor as q , where $m_{\tilde{q}_i}$ denotes their respective masses. The expressions for $a_{\tilde{q}_i}$, $b_{\tilde{q}_i}$ can be found in Ref.[77].

For the Z boson mediated process, the relevant vertex involving $\tilde{\chi}_1^0$ is given by [66, 84],

$$\mathcal{L}_{\tilde{\chi}_1^0 \tilde{\chi}_1^0 Z} = \left(\frac{g_2}{2c_W} \right) \overline{\tilde{\chi}_1^0} \gamma^\mu (\mathcal{N}_{11}^L \mathbf{P}_L + \mathcal{N}_{11}^R \mathbf{P}_R) \tilde{\chi}_1^0 Z_\mu, \quad (20)$$

where,

$$\mathcal{N}_{11}^L = -\frac{1}{2}(|N_{13}|^2 - |N_{14}|^2), \quad (21a)$$

$$\mathcal{N}_{11}^R = -(\mathcal{N}_{11}^L)^*. \quad (21b)$$

In the expressions above N_{13} and N_{14} denote the down-type and up-type Higgsino compositions, respectively, in the mass eigenstate $\tilde{\chi}_1^0$.

For Higgsino-like $\tilde{\chi}_1^0$, we have $|\mu| \ll |M_1|, M_2$. Thus, the gaugino fraction is very small compared to the Higgsino fraction. Further, the mass eigenstate is composed of (approximately) equal proportions of down-type and up-type neutral Higgsino; thus $|N_{13}|^2 - |N_{14}|^2$ is generally small, suppressing the Z mediated contribution. Further, as the squark mediated contributions are proportional to the respective Yukawa couplings, the respective contributions are sub-dominant. Also, as we will discuss in Sec.III, in our work we have considered the (first two generation of) squarks to be very heavy. Therefore, the respective contributions remain sub-dominant. For a Wino-like $\tilde{\chi}_1^0$, M_2 is much smaller than $|\mu|, |M_1|$. Consequently, the Bino and the Higgsino fractions are very small as compared to the Wino fraction. As N_{13} and N_{14} are very small, the tree-level vertex involving Z boson is suppressed in this scenario.¹⁰ The $SU(2)_L$ doublet squark mediated processes, as described above, contribute to the spin-dependent cross-section. As we have assumed these squarks to be heavy in the present work, the contributions remain rather small. It is worth noting that, due to small tree-level cross-section, the radiative corrections to these vertices can be important and can play a crucial role in spin-dependent direct detection processes.

As already mentioned, because of the smallness of the tree-level contributions to the spin-dependent $\tilde{\chi}_1^0$ -nucleus scattering process, it is important to consider radiative corrections. In the next section, we will discuss the radiative corrections to the $\tilde{\chi}_1^0 \tilde{\chi}_1^0 Z$ vertex, which contributes to the coefficient d_q^{tree} , as mentioned above. Further, certain important contributions from the box diagrams involving the electroweak gauge bosons, which were considered in Refs.[37, 39], will also be discussed in the subsequent subsection, as we have incorporated these corrections also for the numerical estimation of the spin-dependent $\tilde{\chi}_1^0$ -nucleus cross-sections.

3. Radiative corrections : $\tilde{\chi}_1^0 \tilde{\chi}_1^0 Z$ vertex

In this section we focus on dominant radiative corrections to the $\tilde{\chi}_1^0 \tilde{\chi}_1^0 Z$ vertex and the relevant counterterms. As discussed in the previous section, the Z -boson mediated $\tilde{\chi}_1^0$ -quark scattering processes contribute

¹⁰ The approximate analytical expressions of the tree-level $\tilde{\chi}_1^0 \tilde{\chi}_1^0 Z$ can be found in Ref.[37]. In this work numerical values for the mixing matrices and the tree-level vertices have been used to precisely estimate the respective contributions for various benchmark scenarios.

substantially to the spin-dependent direct detection. As the tree-level vertex for $\tilde{\chi}_1^0\tilde{\chi}_1^0Z$ is small for almost pure Higgsino-like and Wino-like neutralinos, the radiative corrections can be important for accurate estimation of the spin-dependent direct detection cross-section of $\tilde{\chi}_1^0$.

The radiative corrections to the $\tilde{\chi}_1^0\tilde{\chi}_1^0Z$ vertex generally receive contributions from the gauge bosons, Higgs bosons, neutralinos and charginos, and also from fermion and sfermions running in the loops. For the Higgsino-like $\tilde{\chi}_1^0$ scenario, due to the large Yukawa coupling, the diagrams involving third-generation top quarks and stop squarks provide the most significant radiative contributions. The respective diagrams have been depicted in Fig.1.¹¹ Further, there are sub-dominant contributions from the loops involving two neutralinos (charginos) and Z (W^\pm) bosons. There is some cancellation between the loops involving $\tilde{\chi}_1^+W^+W^+$ and $\tilde{\chi}_1^-W^-W^-$ (shown in Fig.8(a)). Thus, their contribution to the vertex correction remains insignificant, which was also pointed out in Ref.[38]. This cancellation is exact when we take the pure Higgsino (and pure Wino) limit, but when there is a small admixture of Bino and Wino (Bino and Higgsino) in the $\tilde{\chi}_1^0$, i.e., the case considered in this article, this is not an exact cancellation. Further, there is a partial cancellation between the loops involving $\tilde{\chi}_1^+\tilde{\chi}_1^+W^+$ and $\tilde{\chi}_1^-\tilde{\chi}_1^-W^-$ (Fig.8(b)), thus effectively reducing their contributions. Similar to the previous case, this cancellation is exact in the pure Higgsino (and pure Wino) limit. This cancellation is also discussed in Ref.[38]. Note that, in the limit of very heavy gaugino mass parameters, i.e. $|M_1|, M_2 \gg |\mu|$, the dominant contributions from the triangle loops involving two neutralinos and a Z boson are also suppressed by at least one factor of $|N_{i3}|^2 - |N_{i4}|^2$, $i \in \{1, 2\}$. The analytical expressions for different loop diagrams may be found in Appendix A. However, as we will discuss in Sec.III, the contribution, for $|M_1|, M_2 \lesssim 5$ TeV, and for $|\mu| \simeq 1$ TeV, their contribution can be about a few percent compared to the dominant loops.

For a Wino-like neutralino ($M_2 \ll |M_1|, |\mu|$), on the other hand, contributions to the $\tilde{\chi}_1^0\tilde{\chi}_1^0Z$ vertex from the loops involving left-(s)fermions are sizable. However, there are cancellations between the loops involving two fermions and one fermion and the loops involving two sfermions and one fermion of the same flavor. Further, contributions from the loop with two W^+ bosons and one (Wino-like) chargino, and from the loop with the respective anti-particles largely cancel, see also Ref.[37]. Thus, the total contribution from the loops, as well as from the counterterms is not as large as in the Higgsino case.

It is necessary to use a renormalization procedure for the estimation of radiative corrections. We use an appropriate variant of the on-shell renormalization scheme for the chargino-neutralino sector [50–

¹¹ The contributions from the third generation (s)quark loops only, in the context of an almost pure Higgsino-like neutralino, have been discussed in Ref.[36] using $\overline{\text{DR}}$ renormalization scheme, and the effects in the direct detection event rate for very low $\tan\beta \simeq 1.5$ and rather light neutralino mass ($\simeq 70$ GeV), which are dominated by spin-independent cross-section, were presented. Our focus will be primarily on the implications of the $\tilde{\chi}_1^0\tilde{\chi}_1^0Z$ vertex corrections, as evaluated in the on-shell scheme, on the spin-dependent cross-section for both Higgsino-like and Wino-like neutralinos in the parameter region which are consistent with the current experimental constraints.

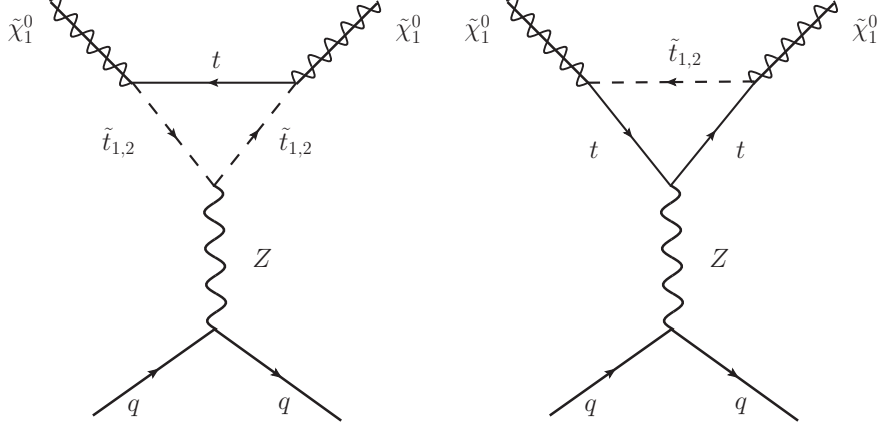


FIG. 1. Feynman diagrams depicting the contributions from the third generation (s)quark sector to the $\tilde{\chi}_1^0 \tilde{\chi}_1^0 Z$ vertex corrections.

52] to renormalize the chargino-neutralino sector. The respective $\tilde{\chi}_1^0 \tilde{\chi}_1^0 Z$ vertex counterterms have been considered, following the implementation in Ref.[85]. As we will discuss in the section III, there are generally large cancellations between the loop corrections and the counterterm contributions to the $\tilde{\chi}_1^0 \tilde{\chi}_1^0 Z$ vertex. To obtain the vertex counterterm, one expresses the “bare” and the renormalized neutralino as

$$\tilde{\chi}_i^0 \text{ bare} = \left(\delta_{ij} + \frac{1}{2} \delta Z_{ij}^L \mathbf{P}_L + \frac{1}{2} \delta Z_{ij}^{R*} \mathbf{P}_R \right) \tilde{\chi}_j^0 \text{ renormalized}, \quad (22)$$

where the index j is summed over $j \in \{1, 2, 3, 4\}$. The wavefunction renormalization counterterms $\delta Z_{ij}^{L/R}$ are determined using on-shell renormalization schemes [50]. A comparison among different choices of the input masses can be found in Ref.[52]. The relevant Lagrangian may be expressed as,

$$\mathcal{L} = \mathcal{L}_{\text{Born}} + \mathcal{L}_{CT}. \quad (23)$$

where the “tree-level” Lagrangian $\mathcal{L}_{\text{Born}}$ is expressed in terms of renormalized fields, and \mathcal{L}_{CT} includes contributions from the relevant counterterms. The counterterm Lagrangian \mathcal{L}_{CT} is given by,

$$-\mathcal{L}_{CT} \supset \overline{\tilde{\chi}_1^0} \gamma^\mu (\delta \mathcal{N}_{11}^L \mathbf{P}_L + \delta \mathcal{N}_{11}^R \mathbf{P}_R) \tilde{\chi}_1^0 Z_\mu. \quad (24)$$

where the values of $\delta \mathcal{N}_{11}^{L/R}$ are given by,

$$\delta \mathcal{N}_{11}^R = \frac{e}{4c_W^3 s_W^2} \left[\sum_{i=1}^4 (\delta Z_{1i}^{R*} + \delta Z_{i1}^R) (N_{13} N_{i3} - N_{14} N_{i4}) s_W c_W^2 - \left((2\delta s_W - (2\delta Z_e + \delta Z_{ZZ}) s_W) c_W^2 - 2\delta s_W s_W^2 \right) \left(|N_{13}|^2 - |N_{14}|^2 \right) \right], \quad (25)$$

and

$$\delta\mathcal{N}_{11}^L = -\frac{e}{4c_W^3 s_W^2} \left[\sum_{i=1}^4 (\delta Z_{1i}^{L*} + \delta Z_{i1}^L) (N_{13} N_{i3} - N_{14} N_{i4}) s_W c_W^2 - \left((2\delta s_W - (2\delta Z_e + \delta Z_{ZZ}) s_W) c_W^2 - 2\delta s_W s_W^2 \right) \left(|N_{13}|^2 - |N_{14}|^2 \right) \right]. \quad (26)$$

In Eqs.(25) and (26), δs_W is the counterterm for s_W , δZ_e is the counterterm corresponding to the electric charge e , and the $\delta Z_{ij}^{L/R}$ correspond to the wavefunction renormalization counterterms, as described in Eq.(22). Further, δZ_{ZZ} is the wavefunction renormalization counterterm for the Z -boson, and is given by,

$$\delta Z_{ZZ} = - \left[\widetilde{\text{Re}} \right] \Sigma_Z^T(M_Z^2), \quad (27)$$

where the square brackets denote that δZ_{ZZ} is diagonal and $\widetilde{\text{Re}}$ takes the real part of loop integrals without affecting the complex couplings, which may be involved. The details of the counterterms in Eqs.(25) and (26) may be found in Refs.[40, 85]. We have closely followed the convention of Refs.[50, 85].

Thus, at one-loop level, the radiative corrections to the $\tilde{\chi}_1^0$ -nucleon interactions receive contributions from the “tree-level” interactions, the loop contributions, and the counterterm contributions. As already discussed, in the present context we will consider radiative corrections to the $\tilde{\chi}_1^0 \tilde{\chi}_1^0 Z$ vertex and the respective vertex counterterms, which contribute substantially to the spin-dependent $\tilde{\chi}_1^0$ - nucleon interactions.

For both Wino-like and Higgsino-like $\tilde{\chi}_1^0$ scenarios, substantial contribution to the spin-dependent $\tilde{\chi}_1^0$ -nucleon come from the electroweak box diagrams (involving the gauge bosons, charginos, neutralinos and quarks), as shown in Fig.5 [37]. The relevant contribution to the effective interaction strength d_q , as described in Eq.(12), d_q^{box} has been discussed in Appendix A following Refs.[37, 39].

III. RESULTS

In this section, we discuss the numerical results. In particular, we evaluate the vertex corrections to the $\tilde{\chi}_1^0 \tilde{\chi}_1^0 Z$ and the respective counterterms in the on-shell renormalization scheme for some benchmark scenarios. Further, important contributions from the electroweak box diagrams have been included in estimating the spin-dependent cross-section following Refs.[37–39, 55]. There are a total of 292 diagrams that are evaluated, composed of six different types of topologies described in Fig.6 in Appendix B. We have checked the UV finiteness of the radiative corrections (comprising of the triangle loop diagrams and the respective vertex counterterms). The results are discussed in the context of the Higgsino-like and the Wino-like $\tilde{\chi}_1^0$ DM.

1. Implementation

We outline the steps followed to compute the $\tilde{\chi}_1^0\tilde{\chi}_1^0Z$ vertex corrections and the improved spin-dependent direct detection cross-section has been presented below. The numerical treatment is similar to the previous work on spin-independent Higgsino scattering with nucleons [40]. The tools `FeynArts-3.11` [85–88], `FormCalc-9.10` [85, 89], `LoopTools-2.16` [89], `SARAH-4.14.5` [90–92], `SPheno-4.0.4` [90, 93], and `micrOMEGAs-5.3.41` [54, 81, 94] are utilized at different stages of the computations:

- First, the Feynman diagrams for the one-loop contributions to the $\tilde{\chi}_1^0\tilde{\chi}_1^0Z$ vertex and the relevant counterterms were evaluated using `FeynArts` and `FormCalc` respectively. The relevant loop integrals were expressed in terms of the Passarino-Veltman (PV) scalar integrals. Subsequently, `Fortran` subroutines were prepared to evaluate the analytical expressions for the vertices and corresponding counterterms numerically.
- Using the spectrum generator `SPheno`, which employs the `SARAH` generated model file for the MSSM, we generated the particle spectrum and the relevant mixing matrices for the benchmark scenarios. Next, we evaluated the numerical values for the vertex corrections and the relevant counterterms using `LoopTools` for the benchmark scenarios. The counterterms are determined using suitable variants of the on-shell renormalization scheme [50–52, 85]. At this stage, we checked that all UV-divergences cancel, yielding a finite result for the $\tilde{\chi}_1^0\tilde{\chi}_1^0Z$ vertex corrections.
- Finally, we updated the $\tilde{\chi}_1^0\tilde{\chi}_1^0Z$ vertex in `micrOMEGAs` by including all the triangular topologies depicted in Fig.6, and these are used to estimate the spin-dependent direct detection cross-section for the benchmark scenarios, as described in Tables I and III.
- Additionally, we incorporate the one-loop diagram shown in Fig.5 to calculate the W/Z box contribution to the neutralino-quark scattering process. While their analytical expressions are available in the literature, they were not previously included in `micrOMEGAs`.

A. Higgsino-Like Neutralino

The lightest neutralinos considered in this study are predominantly Higgsino-like, with a Higgsino fraction of $\gtrsim 99\%$, characterized by $|\mu| \ll |M_1|, M_2$. The Higgsino mass parameter $|\mu|$ is set to 0.3 TeV and 0.6 TeV for the two sets of benchmark points (BP1–BP4). For one benchmark point (BP5), μ is

set to 1.05 TeV to satisfy the thermal relic abundance using tree-level annihilation cross-section. These benchmarks represent the compressed Higgsino spectrum.

In Eq.(20), it is apparent that the tree-level $\tilde{\chi}_1^0 \tilde{\chi}_1^0 Z$ vertex depends on $(|N_{13}|^2 - |N_{14}|^2)$, which is sensitive to the sign and hierarchy of the parameters M_1 and M_2 for a fixed μ , even when $|\mu| \ll |M_1|, M_2$. Consequently, the percentage radiative corrections $\Delta\mathcal{N}^{L/R}$, are sensitive to the sign and the hierarchy of the M_1 and M_2 parameters. Thus, to demonstrate this, the Bino mass parameter M_1 , and the Wino mass parameter M_2 are varied as $(\pm 5, \pm 4)$ TeV and $(4, 5)$ TeV, respectively. In BP5, in order to achieve the thermal relic abundance (using the tree-level annihilation cross-section), M_1 is lowered to -1.3 TeV. The gluino mass parameter M_3 is fixed at 3 TeV to evade the LHC constraints on the mass of gluinos. Additionally, $\tan\beta$ is fixed at 10, and the pseudoscalar Higgs mass is set to 1.414 TeV. The trilinear soft-supersymmetry breaking term involving two stop squarks was assigned as $T_t = -4$ TeV for BP1-BP3 and BP5, while for BP4, it was set to $T_t = 4$ TeV. The soft supersymmetry breaking parameters for BP1-BP3 are: $m_{\tilde{Q}_L} = 2.69$ TeV, $m_{\tilde{t}_R} = 2.06$ TeV. For BP4 and BP5, these parameters are: $m_{\tilde{Q}_L} = 3.50$ TeV, $m_{\tilde{t}_R} = 4.03$ TeV. This variation was done to test the sensitivity of the radiative corrections to the trilinear coupling and the squark masses. Therefore, each choice of the benchmark point represents a different line on the plots in Fig.2, each benchmark indicating a different characteristic of the Higgsino-like $\tilde{\chi}_1^0$ cross-section for the same value of μ parameter. Moreover, all benchmark points successfully pass the collider bounds implemented in `SModelS` (version 2.3.0) [95–103] as well as the direct detection constraints from the LUX-ZEPLIN [28, 104] and the PICO-60 [31] experiments.

The dominant contributions arise from topologies Figs.6(e) and 6(f), which involve loops with top quarks and stop squarks. These loops contribute at a level of $\sim \mathcal{O}(10^{-2})$ to the total vertex factor, which is $\sim \mathcal{O}(10^{-2})$. Contributions from other diagrams within topologies (e) and (f) to the total vertex correction are relatively minor. Specifically, the contributions from bottom quark-sbottom squark loops are of order $\sim \mathcal{O}(10^{-3})$, and diagrams involving other quark/squark flavors, apart from (s)top and (s)bottom, contribute at $\sim \mathcal{O}(10^{-6})$. The combined contributions from loops involving leptons and sleptons in topologies (e) and (f) are of order $\sim \mathcal{O}(10^{-4})$. In Fig.6(a), the topology with $W^\pm W^\pm \tilde{\chi}_i^\pm$ contributes subdominantly, with a value of $\sim \mathcal{O}(10^{-5})$. While the loop involving $W^\pm \tilde{\chi}_i^\pm \tilde{\chi}_j^\pm$ in Fig.6(b) contributes even less, approximately $\mathcal{O}(10^{-6})$. Topologies shown in Figs.6(c) and 6(d) have very small contributions of order $\sim \mathcal{O}(10^{-7})$. Finally, the contribution from diagrams involving both neutral and charged Higgs bosons, as well as electroweakinos in topologies (e) and (f), are negligibly small. For topology (e), they contribute at $\sim \mathcal{O}(10^{-7})$, and for topology (f), the contribution is also of the order $\sim \mathcal{O}(10^{-7})$.

1. Benchmark Scenarios

In this subsection, the benchmark scenarios have been discussed. The benchmark points have been described in Table I. There are a total of nine benchmark points (BP's) that we have discussed in this subsection.

All the required input parameters like μ , M_1 , and M_2 are mentioned in the tables, along with neutralino and chargino tree-level masses (as tree-level masses are used to evaluate the loop vertex factors). The SM-like light Higgs mass is taken as $m_{h_1} = 125 \pm 0.7$ GeV, and m_{h_2} is the mass of the CP-even heavy Higgs. The N_{1i} 's are the neutralino mixing matrix entries mentioned in Eq.(7). HF is the Higgsino fraction of the lightest neutralino $= |N_{13}|^2 + |N_{14}|^2$. It is evident from Table I that the lightest neutralino that we have considered is almost purely Higgsino-like ($\gtrsim 98.8\%$). For BP1, BP2, and BP4, $|M_1|$ and M_2 have not been varied, only the relative sign between M_1 , M_2 , and μ have been varied, and $|M_1| > M_2$. For BP3, $|M_1|$ and M_2 values are interchanged, and $M_2 > |M_1|$. Because of this difference, the renormalization scheme used for these two types of benchmarks is also different. The same is true for BP5 as well. The renormalization scheme used to evaluate the counterterms for benchmarks BP1, BP2, and BP4 is CCN[4], whereas the scheme used for BP3 and BP5 is CCN[3].

The benchmark BP5 (approximately) satisfies the cosmological constraints on the relic density of dark matter with $\Omega h^2 = 0.123$ at this point. This is expected as for the Higgsino-like lightest neutralino, the correct relic density is observed at ~ 1 TeV. All the benchmark points pass the `SModelS` tests as well as the spin-independent direct detection bounds of the LUX-ZEPLIN experiment (LZ) [28, 104], with benchmarks BP1 and BP3-BP5 lying in the 2σ uncertainty band of the most recent LZ results. The spin-independent cross-sections (evaluated using the relevant tree-level vertices involving $\tilde{\chi}_1^0$ in `micrOMEGAs-5.3.41`) are presented in Table II (σ_{SI}^p). The spin-dependent bounds are less stringent, and all the points lie well below the spin-dependent direct detection bounds of PICO-60 [31] (proton) and LZ [28, 104] (proton and neutron).

2. Numerical Results and Discussion

In Table II, $\mathcal{N}^L/\mathcal{N}^R$ are the tree level vertex factors, as mentioned in Eq.(20) for the $\tilde{\chi}_1^0\tilde{\chi}_1^0Z$ vertex, and $\mathcal{N}^L = -\mathcal{N}^R$ for this vertex. $\Delta\mathcal{N}^{L/R} = \frac{\mathcal{N}_{\text{corr.}}^{L/R} - \mathcal{N}_{\text{tree}}^{L/R}}{\mathcal{N}_{\text{tree}}^{L/R}} \times 100$ (%) are the percentage corrections to the tree-level vertex factors. The percentage corrections to the proton and neutron cross-sections are evaluated as $\Delta\sigma_{\text{SD}}^{p/n} = \frac{\sigma_{\text{SD corr.}}^{p/n} - \sigma_{\text{SD tree}}^{p/n}}{\sigma_{\text{SD tree}}^{p/n}} \times 100$ (%). ‘‘Loop’’ refers to the percentage contribution to the tree-level

Parameters	BP1a	BP1b	BP2a	BP2b	BP3a	BP3b	BP4a	BP4b	BP5
μ (GeV)	300	600	-300	-600	300	600	300	600	1050
M_1 (GeV)	-5000	-5000	-4000	-4000	-4000	-4000	-5000	-5000	-1300
M_2 (GeV)	4000	4000	5000	5000	5000	5000	4000	4000	4000
$m_{\tilde{\chi}_1^0}$ (GeV)	299.17	599.06	299.62	599.57	299.44	599.36	299.17	599.06	-1048
$m_{\tilde{\chi}_2^0}$ (GeV)	-300.44	-600.39	-300.4	-600.4	-300.29	-600.24	-300.44	-600.39	1049
$m_{\tilde{\chi}_3^0}$ (GeV)	4002	4002	-4000	-4000	-4000	-4000	4002	4002	-1303
$m_{\tilde{\chi}_4^0}$ (GeV)	-5000	-5000	5001	5001	5001	5001	-5000	-5000	4002
$m_{\tilde{\chi}_1^\pm}$ (GeV)	299.56	599.43	300.18	600.10	299.67	599.58	299.56	599.43	1049
$m_{\tilde{\chi}_2^\pm}$ (GeV)	4002	4002	5001	5001	5001	5001	4002	4002	4002
m_{h_1} (GeV)	125.28	125.25	125.15	125.08	125.19	125.16	125.64	125.53	124.42
m_{h_2} (GeV)	1354	1280	1463.5	1496	1393	1359	1656	1856	901.19
HF	0.9997	0.9996	0.9998	0.9998	0.9998	0.9997	0.9997	0.9996	0.9884
$N_{11}(\times 10^{-3})$	-6.291	5.956	-6.344	-5.933	-7.756	-7.252	-6.291	5.956	107.35
$N_{12}(\times 10^{-2})$	-1.679	1.827	-1.081	-1.156	-1.322	-1.412	-1.679	1.827	1.00
N_{13}	0.708	-0.707	-0.708	-0.707	0.708	0.707	0.708	-0.707	0.704
N_{14}	-0.706	0.707	-0.7065	-0.707	-0.706	-0.707	-0.706	0.707	0.702
$ N_{13} ^2 - N_{14} ^2 (\times 10^{-3})$	2.277	1.279	3.493	0.868	1.537	0.868	2.277	1.279	2.806

TABLE I. The benchmark scenarios with a Higgsino-like $\tilde{\chi}_1^0$ have been tabulated here. HF stands for Higgsino fraction. The trilinear soft-supersymmetry breaking term involving two stop squarks is set as $T_t = -4$ TeV for the benchmarks BP1-BP3 and BP5, and $T_t = 4$ TeV for BP4. The soft supersymmetry breaking parameters for the left and right type squarks and sleptons for BP1-BP3 are as follows: $m_{\tilde{Q}_L} = 2.69$ TeV, $m_{\tilde{t}_R} = 2.06$ TeV, $m_{\tilde{b}_R} = 2.50$ TeV, $m_{\tilde{L}_L} = 2.06$ TeV, and $m_{\tilde{e}_R} = 2.06$ TeV. For BP4 and BP5, these parameters are as follows: $m_{\tilde{Q}_L} = 3.50$ TeV, $m_{\tilde{t}_R} = 4.03$ TeV, and the rest are the same as BP1-BP3. The following input parameters have been fixed for all the benchmark scenarios: $\tan \beta = 10$, $m_A = 1.414$ TeV. The fixed input gluino mass parameter, $M_3 = 3$ TeV. Mass of the Z boson, $M_Z = 91.18$ GeV. For the benchmarks BP1-BP3, the third generation squark mass and mixing parameters remain fixed: the lightest stop mass $m_{\tilde{t}_1} = 2.05$ TeV, the heaviest stop mass $m_{\tilde{t}_2} = 2.71$ TeV, the lightest sbottom mass $m_{\tilde{b}_1} = 2.50$ TeV, the heaviest sbottom mass $m_{\tilde{b}_2} = 2.69$ TeV. For BP4 and BP5, the lightest stop mass $m_{\tilde{t}_1} = 3.49$ TeV, the heaviest stop mass $m_{\tilde{t}_2} = 4.05$ TeV, the lightest sbottom mass $m_{\tilde{b}_1} = 2.50$ TeV, the heaviest sbottom mass $m_{\tilde{b}_2} = 3.50$ TeV. For all the benchmarks, the lightest stau mass $m_{\tilde{\tau}_1} = 2.05$ TeV, and the heaviest stau mass $m_{\tilde{\tau}_2} = 2.08$ TeV. The charged Higgs boson mass $M_{H^\pm} = 1.416$ TeV, the CP-even Higgs mixing angle $\alpha = \sin^{-1}(-0.1)$.

$\tilde{\chi}_1^0 \tilde{\chi}_1^0 Z$ vertex from all the loop diagrams evaluated as $\text{Loop} = \frac{\mathcal{N}_{\text{Loop}}^{L/R}}{\mathcal{N}_{\text{tree}}^{L/R}} \times 100\%$, and ‘‘CT’’ refers to the counter

BP	\mathcal{N}^L ($-\mathcal{N}^R$)	$\Delta\mathcal{N}^{L/R}$ (%) Total (Loop, CT)	W/Z box (%) $a_p(a_n)$ [GeV^{-2}]	σ_{SD}^p [pb] ($\Delta\sigma_{\text{SD}}^p$ %)	σ_{SD}^n [pb] ($\Delta\sigma_{\text{SD}}^n$ %)	σ_{SI}^p [pb]
BP1a	-3.72×10^{-4}	-55.04 (5644, -5699)	12.18 (-16.72) $-1.490 \times 10^{-9} (-1.789 \times 10^{-9})$	6.37×10^{-8} (-67.4)	1.19×10^{-8} (-92.0)	2.79×10^{-11}
BP1b	-2.94×10^{-4}	-36.73 (10050, -10087)	12.52 (-17.22) $-8.604 \times 10^{-10} (-1.035 \times 10^{-9})$	3.55×10^{-8} (-42.6)	1.00×10^{-8} (-83.8)	3.57×10^{-11}
BP2a	-1.66×10^{-4}	-70.23 (8389, -8459)	18.02 (-24.74) $-1.489 \times 10^{-9} (-1.787 \times 10^{-9})$	2.03×10^{-8} (-77.2)	1.17×10^{-10} (-99.7)	4.84×10^{-12}
BP2b	-2.00×10^{-4}	-36.70 (14854, -14891)	18.44 (-25.37) $-8.600 \times 10^{-10} (-1.035 \times 10^{-9})$	1.90×10^{-8} (-33.2)	3.13×10^{-9} (-85.6)	6.23×10^{-12}
BP3a	-1.39×10^{-4}	-75.10 (8382, -8457)	18.02 (-24.74) $-1.489 \times 10^{-9} (-1.788 \times 10^{-9})$	1.64×10^{-8} (-81.6)	2.26×10^{-13} (-100.0)	1.27×10^{-11}
BP3b	-1.73×10^{-4}	-45.11 (14855, -14900)	18.44 (-25.37) $-8.601 \times 10^{-10} (-1.035 \times 10^{-9})$	1.53×10^{-8} (-46.3)	1.90×10^{-9} (-91.3)	1.64×10^{-11}
BP4a	-1.04×10^{-3}	25.31 (6059, -6034)	12.18 (-16.72) $-1.490 \times 10^{-9} (-1.789 \times 10^{-9})$	3.69×10^{-7} (89.0)	1.76×10^{-7} (17.9)	2.67×10^{-11}
BP4b	-6.30×10^{-4}	35.47 (10798, -10762)	12.52 (-17.22) $-8.607 \times 10^{-10} (-1.035 \times 10^{-9})$	1.35×10^{-7} (119.0)	6.61×10^{-8} (39.8)	3.38×10^{-11}
BP5	-1.13×10^{-3}	10.41 (4802, -4792)	3.48 (-4.79) $-5.247 \times 10^{-10} (-6.319 \times 10^{-10})$	3.86×10^{-7} (29.7)	2.54×10^{-7} (11.6)	1.74×10^{-10}

TABLE II. BP refers to the different benchmark points. $\mathcal{N}^L/\mathcal{N}^R$ are the tree level $\tilde{\chi}_1^0\tilde{\chi}_1^0Z$ vertex factors. $\Delta\mathcal{N}^{L/R}$ are the percentage corrections to the tree-level vertex factors. The loop and counterterm contributions are separately given in ‘‘Loop’’ and ‘‘CT’’, respectively. The total contributions from the loops and the counterterms are labelled as ‘‘Total’’; ‘‘W/Z box’’ refers to the percentage contribution to $a_p(a_n)$ from the spin-dependent (SD) component of the W and Z boson box diagrams that have been evaluated, as well as the magnitude of the box contribution to $a_p(a_n)$. The magnitude of the corrected proton (neutron) cross-sections is given as σ_{SD}^p (σ_{SD}^n), and the percentage correction in the spin-dependent proton (neutron) cross-section is given as $\Delta\sigma_{\text{SD}}^p$ ($\Delta\sigma_{\text{SD}}^n$). All the benchmarks pass the `SModelS` checks.

term contribution to the tree-level vertex evaluated with the help of Eq.(25) as $\text{CT} = \frac{\mathcal{N}_{\text{CT}}^{L/R}}{\mathcal{N}_{\text{tree}}^{L/R}} \times 100\%$. The box contribution is evaluated as $W/Z \text{ box } (\%) = \frac{a_{p/n}(\text{box})}{a_{p/n}(\text{tree})} \times 100\%$.¹²

For benchmark points BP1–BP3, we take the soft supersymmetry-breaking parameters $m_{\tilde{Q}_L} = 2.69$ TeV

¹² Note that the sign of the tree-level amplitude for the Z mediated diagram in `micrOMEGAs` has an opposite sign compared to the Ref.[39]; therefore, the relative sign is adjusted for the box diagrams.

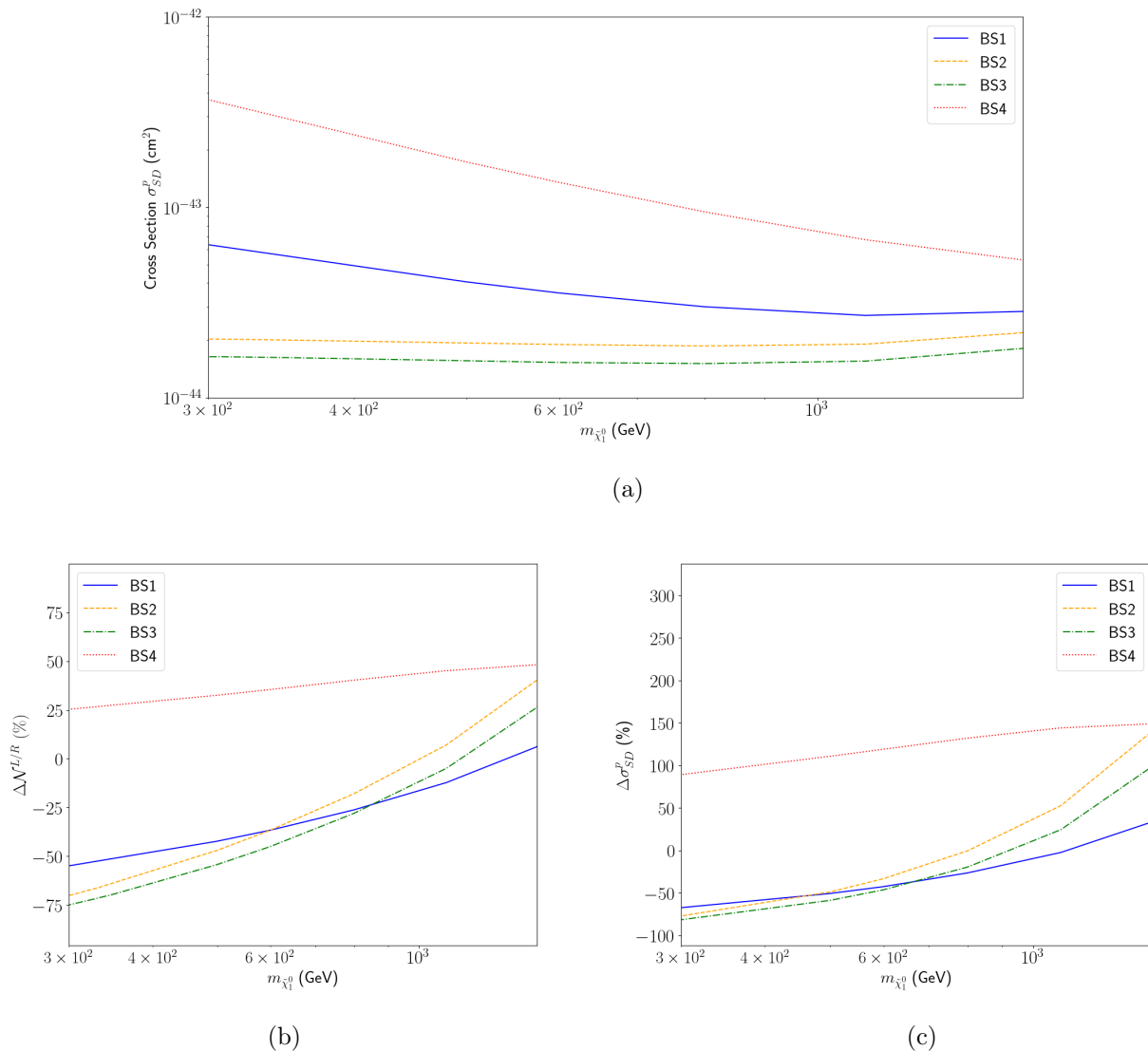


FIG. 2. Panel (a) depicts the variation of the corrected spin-dependent proton cross-section σ_{SD}^p with $m_{\tilde{\chi}_1^0}$ for the benchmark scenarios. Panel (b) illustrates the $\tilde{\chi}_1^0 \tilde{\chi}_1^0 Z$ vertex corrections, $\Delta \mathcal{N}^{L/R}$ (%), varying with respect to $m_{\tilde{\chi}_1^0}$. Panel (c) shows the variation of the proton cross-section corrections, $\Delta \sigma_{SD}^p$ (%), with $m_{\tilde{\chi}_1^0}$. The labels “BS1-BS4” correspond to different benchmark scenarios associated with the benchmark points BP1-BP4. These scenarios represent continuous variations of the μ parameter, while all other parameters remain fixed as specified in Table I. The benchmark points BP1-BP4 lie on these respective lines in the plot. All of the above plots represent the Higgsino-like $\tilde{\chi}_1^0$ scenario.

and $m_{\tilde{t}_R} = 2.06$ TeV, while for BP4–BP5, $m_{\tilde{Q}_L}$ is increased to 3.50 TeV and $m_{\tilde{t}_R}$ to 4.03 TeV. This results in negative vertex and cross-section corrections for BP1–BP3, whereas positive corrections are observed for BP4–BP5. Significant corrections to the $\tilde{\chi}_1^0$ -nucleon cross sections are found for Higgsino-like $\tilde{\chi}_1^0$ benchmark

points. For BP1a, the total vertex correction is a notable -55.04%. Although the combined contribution from all loop diagrams exceeds the tree-level vertex factor by more than 56 times, sizeable cancellation between the loops and counterterms reduces the overall correction. This gauge cancellation pattern is consistent across all benchmark points. The loop-corrected vertex factor is of the order $\mathcal{O}(10^{-4})$ for most benchmarks, except for BP4a and BP5, where it reaches $\mathcal{O}(10^{-3})$. The contribution from electroweak box diagrams (W/Z box) is approximately 12% for the proton (a_p) and -17% for the neutron (a_n) in both BP1a and BP1b. After including the tree-level amplitude with all vertex loop diagrams, counterterms, and box diagram amplitudes, the total proton cross-section correction for BP1a is -67.4%, while the neutron cross-section correction is -92%. The spin-independent cross-section (proton) is of order $\mathcal{O}(10^{-11})$ for all benchmarks, except BP5, where a more mixed state results in a higher cross-section of order $\mathcal{O}(10^{-10})$. In BP1b, the total vertex correction is -36.73%, with proton and neutron cross-section corrections of -42.6% and -83.8%, respectively. For BP2a, the vertex correction is -70.23%, with cross-section corrections of -77.2% (proton) and -99.7% (neutron). The W/Z box contribution is $\sim 18\%$ for the proton and $\sim 25\%$ for the neutron in BP2a and BP2b. In BP2b, the vertex correction is -36.70%, while the cross-section corrections are -33.2% for the proton and -85.6% for the neutron. For BP3a, the $\tilde{\chi}_1^0 \tilde{\chi}_1^0 Z$ vertex correction reaches -75.1%. The W/Z box contribution is around 18% for the proton and -25% for the neutron. The maximum correction for the neutron cross-section is -100% for BP3a, with the proton cross-section correction of -81.6%. In BP3b, the vertex correction is -45.11%, with proton and neutron cross-section corrections of -46.3% and -91.3%, respectively. In BP4a, the vertex correction is 25.31%, with proton and neutron cross-section corrections of 89% and 17.9%, respectively. The box contributions are approximately 12% for the proton and -17% for the neutron for both BP4 benchmarks. BP4b exhibits a vertex correction of 35.47%, with a maximum proton cross-section correction of 119% and a neutron cross-section correction of 39.8%. For BP5, which is a more mixed state, the vertex correction is 10.41%, with cross-section corrections of 29.7% for the proton and 11.6% for the neutron. The box contributions are relatively small, with proton and neutron amplitude corrections of 3.48% and -4.79%, respectively.

In the case of Higgsino-like $\tilde{\chi}_1^0$, the loops involving top quarks and stop squarks are the dominant contributors to the vertex corrections. Each of the two triangular loop diagrams—one involving two top quarks and a stop squark, and the other with two stop squarks and a top quark—contributes with a magnitude of $\gtrsim 0.025$ across all benchmark points. In contrast, the contributions from other diagrams, including those involving quarks, squarks, leptons, and sleptons, are comparatively small at $\lesssim \mathcal{O}(10^{-3})$.

The counterterm contributions are primarily driven by the $\delta Z_{12}^{L/R}$ and $\delta Z_{21}^{L/R}$ terms. While $\delta Z_{12}^{L/R}$ (and $\delta Z_{21}^{L/R}$) and $\delta Z_{11}^{L/R}$ are of comparable magnitude, $\sim \mathcal{O}(10^{-1})$, the $\delta Z_{11}^{L/R}$ term is suppressed by a factor of

($|N_{13}|^2 - |N_{14}|^2$) $\sim 10^{-3}$, as shown in Eqs.(25) and (26). In contrast, $\delta Z_{12}^{L/R}$ and $\delta Z_{21}^{L/R}$ are not subject to this suppression, since $(N_{13}N_{23} - N_{14}N_{24}) \sim 1$. The terms $\delta Z_{i1}^{L/R}$ (and $\delta Z_{1i}^{L/R}$) for $i = 3, 4$ contribute $\mathcal{O}(10^{-4})$ for most benchmarks. Similarly, the counterterms δZ_e and δs_W contribute $\lesssim 10^{-2}$ but are also suppressed by the factor $(|N_{13}|^2 - |N_{14}|^2) \sim 10^{-3}$. Although δZ_{ZZ} has a larger contribution, $\mathcal{O}(10^{-1})$, it is similarly suppressed by the same factor. This suppression pattern remains consistent across all benchmark points.

We have illustrated the results for the Higgsino-like $\tilde{\chi}_1^0$ in Fig.2. The labels ‘‘BS1-BS4’’ in Fig.2 represent different benchmark scenarios corresponding to the benchmark points BP1–BP4. In these scenarios, the μ parameter, and thus, $m_{\tilde{\chi}_1^0}$ is varied, while all other parameters remain fixed as listed in Table I. The benchmark points BP1–BP4 are located on their respective lines in the plot. In Fig.2(a), shows the variation of the corrected spin-dependent proton cross-section (σ_{SD}^p) with $m_{\tilde{\chi}_1^0}$ in the Higgsino-like scenario. In Fig.2(b), the variation of the percentage vertex correction of the $\tilde{\chi}_1^0 \tilde{\chi}_1^0 Z$ vertex ($\Delta \mathcal{N}^{L/R}$) is illustrated with $m_{\tilde{\chi}_1^0}$ for different Higgsino-like benchmarks. Similarly, in Fig.2(c), the variation of the percentage proton cross-section correction ($\Delta \sigma_{SD}^p$) is shown with $m_{\tilde{\chi}_1^0}$ for various Higgsino-like benchmarks. The various lines on the plot show the different benchmark scenarios where for the same value of the $m_{\tilde{\chi}_1^0}$, different values of the cross-section and vertex corrections are observed, emphasising the importance of the choice of benchmarks.

B. Wino-like Neutralino

In the scenario where the lightest neutralino is almost purely Wino-like, the tree-level $\tilde{\chi}_1^0 \tilde{\chi}_1^0 Z$ vertex becomes negligible, and radiative corrections may become significant. Such a scenario is considered in the following subsection where $M_2 \ll |M_1|, |\mu|$, with a Wino fraction of $\gtrsim 99.9\%$. It is apparent from Eq.(20) that the tree-level $\tilde{\chi}_1^0 \tilde{\chi}_1^0 Z$ vertex depends on $(|N_{13}|^2 - |N_{14}|^2)$, which is sensitive to the sign and the hierarchy of M_1 and μ parameters for a fixed M_2 . Consequently, the relative importance of the radiative corrections to the $\tilde{\chi}_1^0 \tilde{\chi}_1^0 Z$ vertex can significantly vary with the choice of M_1 and μ parameters, even when $M_2 \ll |M_1|, |\mu|$. To demonstrate this, for each benchmark point, M_2 is varied between 1.5 TeV and 1.8 TeV, while M_1 and μ are varied between $(\pm 4, \pm 5)$ TeV. We have considered various combinations of M_1 , M_2 , and μ across different benchmark scenarios. In particular, BP6 and BP10 correspond to the hierarchy $|M_1| > |\mu|$, while BP7 to BP9 represent cases where $|M_1| = |\mu|$. For benchmarks with the same mass hierarchy between $|M_1|$ and $|\mu|$, we explore different relative signs between M_1 , M_2 , and μ to capture a broader range of phenomenological effects. M_3 is kept fixed at 3.5 TeV to evade the LHC collider constraints

on the mass of gluinos, with $\tan\beta$ set at 10 and the pseudoscalar Higgs mass held constant at 3.46 TeV. Each benchmark scenario corresponds to a different line on the plot in Fig.3, further emphasising the significance of the benchmarks. All benchmark points satisfy the collider constraints imposed by `SModelS` (version 2.3.0) [95–103] as well as the direct detection bounds from LZ [28, 104]. The benchmark BP10 lies in the 2σ uncertainty band for the spin-independent case. The spin-independent cross-sections (evaluated using the relevant tree-level vertices involving $\tilde{\chi}_1^0$) are presented in Table IV (σ_{SI}^p).

In the Wino case, the topology shown in Fig.6(a), which involves $W^\pm W^\pm \tilde{\chi}_i^\pm$, is one of the dominant contributors, with a contribution of $\sim \mathcal{O}(10^{-5})$ to the total vertex corrections (which are of order $\sim \mathcal{O}(10^{-5})$). The other dominant contribution comes from loops involving top quarks and stop squarks with both Figs.6(e) and 6(f) contributing up to $\mathcal{O}(10^{-3})$. But there is a cancellation between these figures and the total contribution is of $\mathcal{O}(10^{-5})$. The $W^\pm \tilde{\chi}_i^\pm \tilde{\chi}_j^\pm$ loop in Fig.6(b) contributes $\sim \mathcal{O}(10^{-6})$. The topologies in Fig.6(c) and 6(d) have a much smaller contribution, of the order of $\sim \mathcal{O}(10^{-8})$. Other diagrams corresponding to topologies (e) and (f) contribute relatively less to the total vertex correction. The combined contributions from bottom-sbottom loops are of order $\sim \mathcal{O}(10^{-6})$, and contributions from all loops with other flavors of quarks/squarks (apart from (s)top and (s)bottom) are of the order $\mathcal{O}(10^{-8})$. Diagrams involving leptons and sleptons in topologies (e) and (f) contribute at $\sim \mathcal{O}(10^{-7})$. Diagrams involving both neutral and charged Higgses, as well as electroweakinos, in topology (e) contribute negligibly, at the level of $\sim \mathcal{O}(10^{-9})$. Topology (f) diagrams, however, contribute more significantly, at approximately $\mathcal{O}(10^{-6})$.

1. Benchmark Scenarios

In this subsection, the Wino-like benchmark scenarios have been discussed. The benchmark points have been described in Table III.

The relic density of the Wino-like $\tilde{\chi}_1^0$ is satisfied considering the (co-)annihilation processes at the tree-level for $M_2 \sim 1.8$ TeV for the benchmark point BP10.¹³ At the tree-level, the mass splitting between $\tilde{\chi}_1^0$ and $\tilde{\chi}_1^\pm$, i.e., $\Delta m = m_{\tilde{\chi}_1^\pm} - m_{\tilde{\chi}_1^0}$ is very small, $\sim \mathcal{O}(0.1)$ MeV. The small Δm leads to the $\tilde{\chi}_1^\pm$ not decaying to the $\tilde{\chi}_1^0$ and coannihilation happens for the $\tilde{\chi}_1^\pm$ as well as the $\tilde{\chi}_1^0$, thus the relic density is increased. This leads to the correct relic density of $\Omega h^2 \simeq 0.12$ at a lower M_2 value of 1.8 TeV. However, when the on-shell

¹³ As mentioned in footnote 4, including Sommerfeld enhancement, the thermal relic is achieved at $M_2 \sim 2.7 - 3$ TeV [58–60, 62]. We have not considered this effect in the analysis of the Higgsino-like and Wino-like $\tilde{\chi}_1^0$. However, we have checked for a benchmark point with $M_2 = 2.7$ TeV (sfermion masses are increased to 3-4 TeV to ensure $\tilde{\chi}_1^0$ is the LSP, keeping other parameters similar to BP10), that the vertex correction is $\sim 8\%$ and the cross-section correction is $\sim 70\%$, which is dominated by the electroweak box diagrams. The results are sensitive to the choice of M_1 and μ . Thus, qualitatively, we observe a similar trend regarding relative importance of the radiative corrections to the spin-dependent direct detection of Wino-like DM with $m_{\tilde{\chi}_1^0} \simeq 2.7 - 3$ TeV.

Parameters	BP6	BP7	BP8	BP9	BP10
M_2 (GeV)	1500	1500	1550	1600	1800
M_1 (GeV)	-5000	5000	-5000	-5000	5000
μ (GeV)	-4000	5000	5000	-5000	4000
$m_{\tilde{\chi}_1^0}$ (GeV)	1500	1499	1549	1600	1799
$m_{\tilde{\chi}_2^0}$ (GeV)	-4000	4967	-4973	-4967	-4000.5
$m_{\tilde{\chi}_3^0}$ (GeV)	4001	-5000	5001	5001	4001
$m_{\tilde{\chi}_4^0}$ (GeV)	-5001	5034	-5028	-5034	5001
$m_{\tilde{\chi}_1^\pm}$ (GeV)	1500	1499	1549	1600	1799
$m_{\tilde{\chi}_2^\pm}$ (GeV)	4002	5002	5002	5001	4002
m_{h_1} (GeV)	124.39	125.70	125.79	124.18	125.53
m_{h_2} (GeV)	4108	2743	2495	4205	2894
WF	0.9995	0.9996	0.9996	0.9997	0.9991
$N_{11}(\times 10^{-5})$	2.742	-10.83	-5.943	1.426	-21.96
N_{12}	0.9997	0.9998	-0.9998	0.9998	0.9996
$N_{13}(\times 10^{-2})$	2.238	-1.809	1.823	1.724	-2.617
$N_{14}(\times 10^{-3})$	6.392	7.025	-7.248	3.918	13.77
Ωh^2	0.092	0.092	0.098	0.110	0.121

TABLE III. The benchmark scenarios with a Wino-like $\tilde{\chi}_1^0$ have been tabulated above. WF stands for Wino fraction = $|N_{12}|^2$. Ωh^2 is the thermal relic density of the lightest neutralino in the early universe. The trilinear soft-supersymmetry breaking term involving two stop squarks is set as $T_t = -4$ TeV for the given benchmarks. The pseudoscalar Higgs mass parameter $m_A = 3.46$ TeV. The soft supersymmetry breaking parameters for the left and right type squarks and sleptons are as follows: $m_{\tilde{Q}_L} = 2.7$ TeV, $m_{\tilde{t}_R} = 3.05$ TeV, $m_{\tilde{b}_R} = 3.50$ TeV, $m_{\tilde{L}_L} = 3.05$ TeV, and $m_{\tilde{e}_R} = 2.05$ TeV. The following input parameters have been fixed for all the benchmark scenarios: $\tan \beta = 10$, the fixed input gluino mass parameter $M_3 = 3.5$ TeV, and the mass of the Z boson $M_Z = 91.18$ GeV. The third generation squark mass and mixing parameters remain fixed: the lightest stop mass $m_{\tilde{t}_1} = 2.65$ TeV, the heaviest stop mass $m_{\tilde{t}_2} = 3.10$ TeV, the lightest sbottom mass $m_{\tilde{b}_1} = 2.69$ TeV, and the heaviest sbottom mass $m_{\tilde{b}_2} = 3.50$ TeV. For all the benchmarks, the lightest stau mass $m_{\tilde{\tau}_1} = 2.06$ TeV, and the heaviest stau mass $m_{\tilde{\tau}_2} = 3.05$ TeV. The charged Higgs boson mass $M_{H^\pm} = 3.465$ TeV, and the CP-even Higgs mixing angle $\alpha = \sin^{-1}(-0.1)$.

masses for the charginos and neutralinos are taken as the physical mass, then we get an increased mass splitting of $\Delta m = 155$ -160 MeV. Then, the $\tilde{\chi}_1^\pm$ is no longer stable and can decay to $\tilde{\chi}_1^0$ and an electron. Thus, the benchmarks are not ruled out by stable charged particle constraints. The tree-level as well as the on-shell mass splitting Δm is large for the case of Higgsino-like $\tilde{\chi}_1^0$, $\Delta m = 0.05$ -8 GeV. Therefore, the

$\tilde{\chi}_1^\pm$ is not stable for the tree-level or the on-shell mass. Thus, for the almost pure Higgsino-like $\tilde{\chi}_1^0$, the correct relic density is achieved at the standard value of ~ 1 TeV.

2. Numerical Results and Discussion

In the Wino-like $\tilde{\chi}_1^0$ scenario, in order to evade the LHC (`SModelS`) constraints, M_2 has been considered $\gtrsim 0.65$ TeV [18]. To probe the relic density satisfying parameter region, the Wino mass parameter is raised to 1.5 TeV and above. This leads to more mixing between the electroweakinos, resulting in a relatively large tree-level amplitude. Hence, we see a diminished relative contribution from the vertex loop diagrams and the counterterms as compared to the Higgsino-like scenario. The vertex corrections are still phenomenologically significant and can exceed 15% of the tree-level vertex. However, the most significant contribution here comes from the electroweak box diagrams or the W/Z box diagrams shown in Fig.5. It is important to note here that from Eq.(A.3), it is evident that when $Y = 0$, which is the case for a Wino-like $\tilde{\chi}_1^0$, the contribution from the Z boson box diagram vanishes. Thus, only the W boson box diagram is responsible for the W/Z box contribution in the cross-section corrections in the Wino-like $\tilde{\chi}_1^0$ scenario.¹⁴

The results of the radiative corrections for the Wino-like neutralino are summarized in Table IV. The corrected vertex factors for all benchmark scenarios are of $\mathcal{O}(10^{-4})$. Notably, the loop and counterterm contributions remain small in these cases, and the large gauge cancellation observed in the Higgsino-like scenario is absent in the Wino-like case.

For BP6, the $\tilde{\chi}_1^0\tilde{\chi}_1^0Z$ vertex correction is 3.11%, while the W boson box contribution is significant, resulting in a 77.66% amplitude correction for the proton and -30.54% for the neutron coming from the box diagram. Consequently, the total proton cross-section experiences a 231.3% correction, whereas the total neutron cross-section undergoes a -49.6% correction. The spin-independent proton cross-section is $\mathcal{O}(10^{-12})$, ranging from $\mathcal{O}(10^{-13})$ to $\mathcal{O}(10^{-11})$ across different benchmarks. In the BP7 benchmark, the vertex correction is 14.13%, with the largest box contribution seen in this case: 173.3% for the proton and -37.68% for the neutron. This leads to the most substantial cross-section correction, with a 799.6% increase for the proton and a -54.6% reduction for the neutron. For BP8, the vertex correction is 10.69%, and the W boson box correction reaches approximately 165% for the proton and -35.6% for the neutron. This results in a 717.35% proton cross-section correction and -53.6% for the neutron. In the BP9 benchmark, the vertex correction is 15.20%, and the box contributions are 154.65% for the proton and -33.26% for the neutron. The resulting cross-section corrections are 721.2% for the proton and -48.7% for the neutron.

¹⁴ Note that, as before, the sign of the tree-level amplitude for the Z mediated diagram in `micrOMEGAs` has an opposite sign compared to the Ref.[39]; therefore, the relative sign is adjusted for the box diagrams.

BP	\mathcal{N}^L ($-\mathcal{N}^R$)	$\Delta\mathcal{N}^{L/R}$ (%) Total (Loop, CT)	W/Z box (%) $a_p(a_n)$ [GeV^{-2}]	σ_{SD}^p [pb] ($\Delta\sigma_{SD}^p$ %)	σ_{SD}^n [pb] ($\Delta\sigma_{SD}^n$ %)	σ_{SI}^p [pb]
BP6	-1.72×10^{-4}	3.11 (-0.24, 3.35)	77.66 (-30.54) -1.37×10^{-9} (-1.37×10^{-9})	1.36×10^{-8} (231.3)	1.34×10^{-8} (-49.6)	3.70×10^{-12}
BP7	-1.15×10^{-4}	14.13 (13.80, 0.33)	173.30 (-37.68) -1.37×10^{-9} (-1.37×10^{-9})	7.41×10^{-9} (799.6)	7.91×10^{-9} (-54.6)	1.93×10^{-11}
BP8	-1.13×10^{-4}	10.69 (13.30, -2.61)	165.88 (-35.61) -1.33×10^{-9} (-1.33×10^{-9})	6.92×10^{-9} (717.35)	8.52×10^{-9} (-53.6)	2.04×10^{-11}
BP9	-1.18×10^{-4}	15.20 (11.76, 3.45)	154.65 (-33.26) -1.29×10^{-9} (-1.29×10^{-9})	7.19×10^{-9} (721.2)	9.98×10^{-9} (-48.7)	9.56×10^{-13}
BP10	-1.90×10^{-4}	5.78 (8.67, -2.89)	58.18 (-21.61) -1.16×10^{-9} (-1.16×10^{-9})	1.44×10^{-8} (175.1)	2.48×10^{-8} (-34.6)	6.58×10^{-11}

TABLE IV. BP refers to the different benchmark points. $\mathcal{N}^L/\mathcal{N}^R$ are the tree level vertex factors. $\Delta\mathcal{N}^{L/R}$ are the percentage corrections to the tree-level vertex factors. The loop and counterterm contributions are separately given in “Loop” and “CT”, respectively, as in Table II. The total contributions from the loops and the counterterms are labelled as “Total”; “ W/Z box” refers to the percentage contribution to $a_p(a_n)$ from the spin-dependent (SD) component of the W and Z boson box diagrams that have been evaluated in Eq.(A.1), as well as the magnitude of the box contribution to $a_p(a_n)$. The magnitude of the corrected proton (neutron) cross-section is given as σ_{SD}^p (σ_{SD}^n), the percentage correction in the spin-dependent proton (neutron) cross-section is given as $\Delta\sigma_{SD}^p$ ($\Delta\sigma_{SD}^n$).

Finally, in BP10, the vertex correction is 5.78%, with box contributions of 58.18% for the proton and -26.61% for the neutron, resulting in a proton cross-section correction of 175.1% and a neutron correction of -34.6%. As illustrated in Table IV, the box contribution depends solely on the mass of the $\tilde{\chi}_1^0$, and shows no dependence on the parameters M_1 and μ . This is evidenced by the identical magnitude of the box amplitude for the pair of benchmarks BP6 and BP7.

In the Wino-like $\tilde{\chi}_1^0$ scenario, as in the Higgsino-like case, the dominant loop contributions arise from the top quark and stop squark loops. Specifically, the triangular loop diagrams—one involving two top quarks and a stop squark, and the other involving two stop squarks and a top quark—both contribute with a magnitude of $\mathcal{O}(10^{-3})$. However, unlike the Higgsino case, these two triangle diagrams interfere destructively, resulting in an overall contribution of $\mathcal{O}(10^{-5})$. Despite this cancellation, these are still the dominant loop contributions, as the total loop contribution in the Wino-like $\tilde{\chi}_1^0$ scenario remains $\mathcal{O}(10^{-5})$. The next significant contribution comes from the W boson loops. The loops involving two W bosons

and one chargino, along with those involving two charginos and one W boson, contribute at the order of $\mathcal{O}(10^{-5})$ to the vertex corrections. All other vertex diagrams involving particles such as leptons, sleptons, quarks, squarks, and Higgs bosons contribute subdominantly.

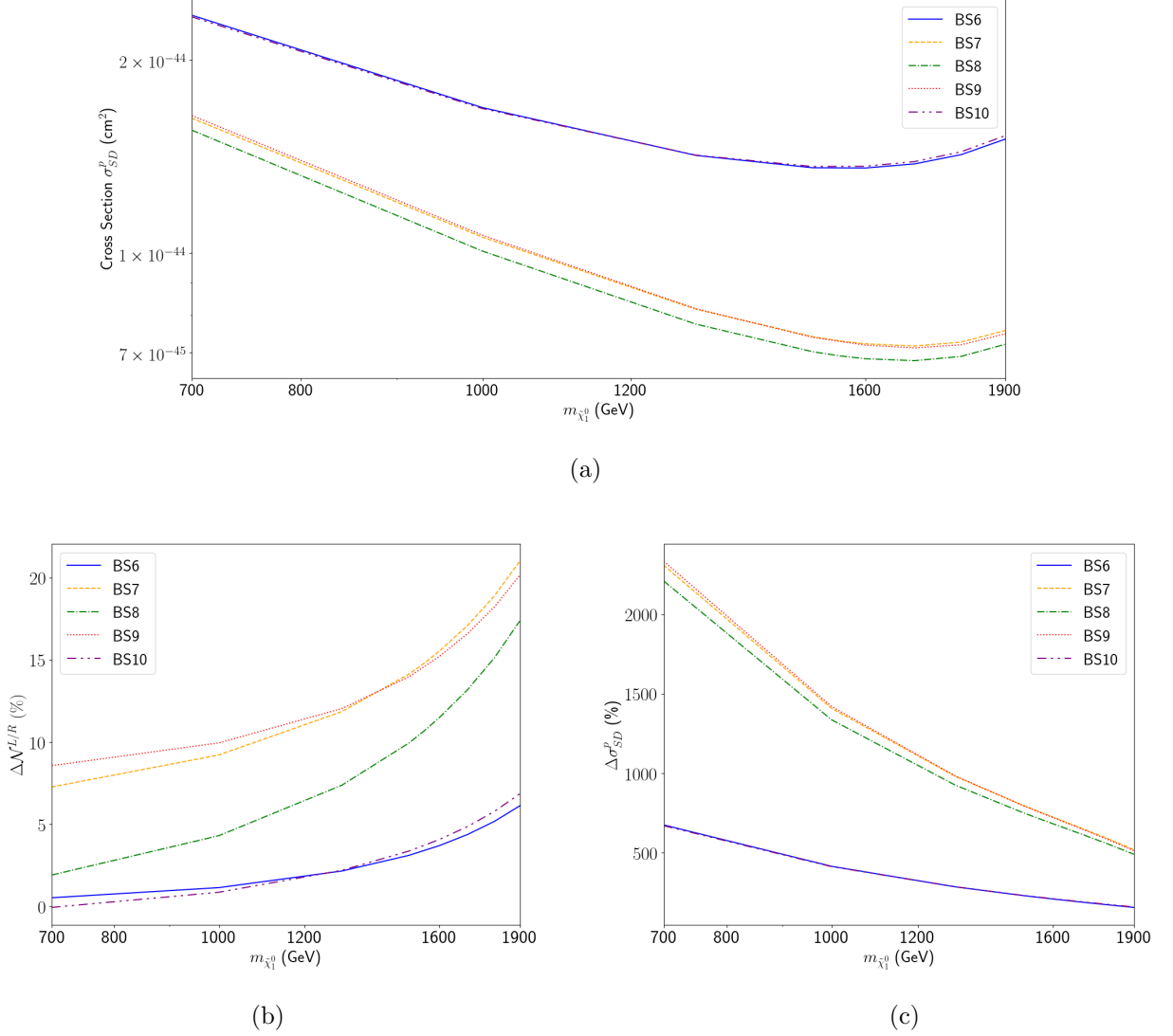


FIG. 3. This figure represents the parameter plots for the Wino-like $\tilde{\chi}_1^0$ scenario. Panel (a) depicts the variation of the corrected spin-dependent proton cross-section σ_{SD}^p with $m_{\tilde{\chi}_1^0}$. Panel (b) illustrates the $\tilde{\chi}_1^0 \tilde{\chi}_1^0 Z$ vertex corrections, $\Delta \mathcal{N}^{L/R}$ (%), varying with respect to $m_{\tilde{\chi}_1^0}$. Panel (c) shows the variation of the proton cross-section corrections, $\Delta \sigma_{SD}^p$ (%), with $m_{\tilde{\chi}_1^0}$. Similar to Fig.2, the “BS6-BS10” labels mean the benchmark scenarios corresponding to the benchmark points BP6-BP10, respectively, and only M_2 is varied for those particular lines keeping all the other parameters same as given in Table III.

For the counterterm contributions, the $\delta Z_{11}^{L/R}$ term contributes up to $\mathcal{O}(10^{-1})$. However, it is suppressed

by a factor of $(|N_{13}|^2 - |N_{14}|^2) \sim \mathcal{O}(10^{-4})$. On the other hand, the $\delta Z_{12}^{L/R}$ (and $\delta Z_{21}^{L/R}$) terms contribute up to $\mathcal{O}(10^{-3})$, but are multiplied by a factor of $(N_{13}N_{23} - N_{14}N_{24}) \sim \mathcal{O}(10^{-2})$ for benchmarks with $|M_1| > |\mu|$ (i.e., BP6 and BP10), which is less suppressed for a Higgsino-like $\tilde{\chi}_2^0$. Therefore, in such a scenario, both these terms end up contributing at a similar order. The terms involving $\delta Z_{13}^{L/R}$ and $\delta Z_{14}^{L/R}$ also contribute $\lesssim \mathcal{O}(10^{-3})$, but are usually subdominant compared to $\delta Z_{12}^{L/R}$. In the benchmarks with $|M_1| = |\mu|$, i.e., BP7-BP9, the factor $(N_{13}N_{23} - N_{14}N_{24}) \sim \mathcal{O}(10^{-3})$ and is smaller than the factor $(N_{13}N_{33} - N_{14}N_{34}) \sim \mathcal{O}(10^{-2})$ which multiplies the $\delta Z_{13}^{L/R}$ term. Therefore, in these benchmarks the $\delta Z_{11}^{L/R}$ and $\delta Z_{13}^{L/R}$ terms dominate, while $\delta Z_{12}^{L/R}$ and $\delta Z_{14}^{L/R}$ are suppressed. In the second term of the counterterm equations (25) and (26), the δZ_{ZZ} term is dominant, with a contribution of $\mathcal{O}(10^{-1})$. However, this term is also suppressed by a factor of $(|N_{13}|^2 - |N_{14}|^2) \sim \mathcal{O}(10^{-4})$. Finally, the terms proportional to δs_W and δZ_e contribute around $\mathcal{O}(10^{-2})$, but they are suppressed as $(|N_{13}|^2 - |N_{14}|^2)$ (see Eqs.(25) and (26)). This suppression pattern holds consistently for all benchmark points.

We have illustrated the results in Fig.3 for the Wino-like $\tilde{\chi}_1^0$. Fig.3(a) illustrates the variation of corrected proton cross-section (σ_{SD}^p) with the $\tilde{\chi}_1^0$ mass. The ‘‘BS6-BS10’’ legends in Fig.3 indicate that the benchmark points BP6-BP10 lie on their corresponding lines ‘‘BS6-BS10’’ in the plot. In these cases, only M_2 is varied, while all other parameters remain fixed as listed in Table III. Fig.3(b) and Fig.3(c) illustrate the variation of vertex correction and proton cross-section correction respectively, with $\tilde{\chi}_1^0$ mass, for different Wino-like benchmarks. The vertex corrections are increasing with mass of $\tilde{\chi}_1^0$ but the cross-section corrections are decreasing with increasing $m_{\tilde{\chi}_1^0}$ (M_2 parameter). This is due to the W boson box diagram contributions, which are inversely related to the mass of $\tilde{\chi}_1^0$, and are the dominant contributors to the cross-section corrections (see Appendix A, especially Eqs.(A.3) and (A.6)). The corrections vary smoothly for each benchmark scenario, which further demonstrates the significance of the choice of benchmark points.

C. Comparison with direct detection experiments

The comparison of the corrected cross-section plots for the Higgsino-like and Wino-like $\tilde{\chi}_1^0$ with some prominent current and future direct detection experimental bounds is shown in Fig.4. The results of this work are compared with the most recent bounds of LZ experiment [104], the proposed limits of the ongoing XENONnT experiment [106], and proposed limits of the future experiments of PandaX-xT [105] and DARWIN [107]. The cross-section bounds for the proton case is not mentioned in the DARWIN experiment’s proposed plots, therefore it is not shown in Fig.4. All of the benchmark points lie below the current and future direct detection experimental limits apart from BP4a, which lies beyond the

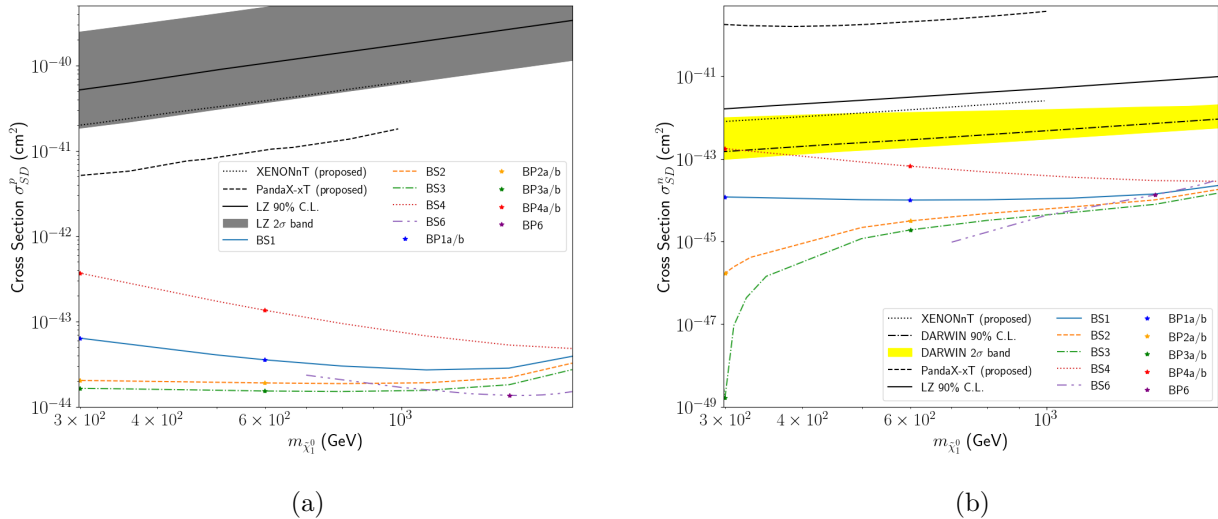


FIG. 4. Panels (a) and (b) illustrate the comparison of the Higgsino-like (and Wino-like) $\tilde{\chi}_1^0$ corrected cross-section comparison with current and future direct detection bounds for proton and neutron cross-sections, respectively. The “BS1-BS6” legend labels correspond to the benchmark scenarios related to the benchmark points BP1-BP6, respectively. BP1-BP6 benchmark points (apart from BP5) are also plotted along with the benchmark scenarios, for reference. The LZ bounds are taken from Ref.[104], PandaX-xT future experiment’s proposed limits are taken from Ref.[105], the XENONnT proposed limits are from Ref.[106] and the proposed limits for the future direct detection experiment DARWIN are taken from Ref.[107].

proposed 90% C.L. of the DARWIN experiment, but still lies within the 2σ uncertainty band. Thus, all the benchmarks are safe from experimental exclusion. The Wino-like $\tilde{\chi}_1^0$ cross-sections are much smaller than their Higgsino-like counterparts, and lie well below the experimental bounds. Thus, only one of the benchmark scenarios, i.e., BS6 (BP6) has been shown in the Figure, which has the maximum corrected cross-section in the Wino-like case. In this context, note that the respective (tree-level) spin-independent cross-sections for all the benchmark points except BP6 and BP9 can be probed, for example, in the proposed experiment DarkSide-20k [108].

IV. CONCLUSION

To summarize, in this article we have explored the implications of important radiative corrections to the spin-dependent interaction of Higgsino-like and Wino-like neutralino $\tilde{\chi}_1^0$ DM with nuclei. In particular, we considered the radiative corrections to the $\tilde{\chi}_1^0 \tilde{\chi}_1^0 Z$ vertex, and evaluated the triangle loops and the respective vertex counterterms in appropriate versions of the on-shell renormalization scheme. We then

studied the implication of the vertex corrections to the spin-dependent direct detection of the $\tilde{\chi}_1^0$ DM. Further, we added contributions from important electroweak box diagrams, which have been previously studied in the literature, to estimate the impact of the radiative corrections to the spin-dependent $\tilde{\chi}_1^0$ -nucleon direct detection cross-section.

Specifically, for the benchmark scenarios with Higgsino-like $\tilde{\chi}_1^0$ substantial corrections to the tree-level $\tilde{\chi}_1^0\tilde{\chi}_1^0Z$ vertex are observed, with maximum corrections of approximately -75% for the Higgsino-like case and 15% for the Wino-like case. At the cross-section level, these corrections can lead to changes of up to $\sim -93.5\%$ and 57% for the Higgsino- and Wino-like scenarios, respectively. Including the electroweak box diagram contributions, we observe cross-section corrections of approximately 119% (-100%) in the Higgsino-like case, and 800% (-55%) for the Wino-like case in the proton (neutron) cross-sections. These highlight the crucial impact of radiative corrections on the spin-dependent cross-sections for neutralino dark matter. The significant enhancement or suppression in interaction strength at the loop level, compared to the tree level, indicates that neglecting these corrections could lead to substantial under- or overestimations of detection rates in direct detection experiments.

For Higgsino-like $\tilde{\chi}_1^0$, the vertex corrections are sizable. Further, there is a large cancellation between the triangle loop contributions and the counterterm contributions evaluated using the on-shell renormalization scheme. Note that, in this case, the suppression of the $\tilde{\chi}_1^0\tilde{\chi}_1^0Z$ vertex is attributed to a cancellation between the mixing matrix elements N_{13} and N_{14} , which corresponds to the down-type and up-type Higgsino gauge eigenstate components to $\tilde{\chi}_1^0$. Thus the suppression of the tree-level vertex is generally also sensitive to the gaugino mass parameters. This has been demonstrated by varying the gaugino mass parameters for the same Higgsino mass parameter μ in different benchmark scenarios. Among the triangle loops, largest contribution comes from the loops involving (s)top (s)quarks, thanks to the large Yukawa coupling. The overall vertex correction is sensitive to the stop mass and mixing parameters including the tri-linear soft-supersymmetry breaking term. This feature has been explored in different benchmark scenarios. As for the counterterms, the largest contribution comes from the off-diagonal wavefunction renormalization constant δZ_{12} , which receives large contribution from the (s)top sector for the same reason as stated above. For Wino-like $\tilde{\chi}_1^0$, the total effect of the vertex corrections is generally much smaller than that of the electroweak box contributions, which dominate. Note that the loop contributions are also suppressed by the Wino-Higgsino mixing.

The benchmark scenarios demonstrate the significance of radiative corrections on the spin-dependent cross-sections for Higgsino-like (and also Wino-like) $\tilde{\chi}_1^0$. These corrections may enhance or deplete the spin-dependent cross-sections. While in the parameter region of interest, the estimated spin-dependent

cross-section is much smaller than that of the experimental limits, it is nevertheless useful to estimate the spin-dependent $\tilde{\chi}_1^0$ -nucleus scattering cross-sections accurately, which can be relevant in the light of future experiments. The present study, therefore, highlights the significance of radiative corrections to the spin-dependent $\tilde{\chi}_1^0$ -nucleus interactions.

ACKNOWLEDGEMENT

The computations were supported in part by SAMKHYA, the High-Performance Computing Facility provided by the IoP, Bhubaneswar, India. The authors acknowledge useful discussions with A. Pukhov. A.C. acknowledges the hospitality at IoP, Bhubaneswar, during the meeting IMHEP-19 and IMHEP-22 which facilitated this work. A.C. and S.A.P. also acknowledge the hospitality at IoP, Bhubaneswar, during a visit. S.B. acknowledges the local hospitality at SNIoE, Greater Noida, during the meeting at WPAC-2023 where this work was put in motion. S.B. and D.D. also acknowledge the local hospitality received at SNIoE, Greater Noida, during the final stage of the work.

APPENDIX A

A. W and Z Box Contribution

The W/Z box diagrams also contribute towards the direct detection process of neutralino dark matter. The W and Z boson box diagrams as shown in Fig.5, play a role in the enhancing (or reducing) the spin-dependent cross-section of the $\tilde{\chi}_1^0\tilde{\chi}_1^0Z$ vertex. The coefficient of the amplitude of the neutralino-quark scattering via the W and Z box diagrams is given as [38, 39]

$$a_N = \sum_{q=u,d,s} d_q \Delta q_N \quad (\text{A.1})$$

(where $N = p, n$), and

$$d_q = d_q^{\text{tree}} + d_q^{\text{box}}, \quad (\text{A.2})$$

where

$$d_q^{\text{box}} = \frac{n^2 - (4Y^2 + 1)}{8} \frac{\alpha_2^2}{m_W^2} g_{AV}(w) + \frac{2((a_q^V)^2 - (a_q^A)^2)Y^2}{\cos^4 \theta_W} \frac{\alpha_2^2}{m_Z^2} g_{AV}(z). \quad (\text{A.3})$$

Here, m_W and m_Z are the masses of W and Z bosons respectively, and $\alpha_2^2 = g_2^2/4\pi$. The coupling of

quarks with Z boson (vector and axial-vector) is given as

$$a_q^V = \frac{1}{2}T_{3q} - Q_q \sin^2 \theta_W, \quad a_q^A = -\frac{1}{2}T_{3q}. \quad (\text{A.4})$$

Here, T_{3q} and Q_q represent the weak isospin and charge of quark q , respectively. Further, we parametrize $w = m_W^2/m_{\tilde{\chi}_1^0}^2$ and $z = m_Z^2/m_{\tilde{\chi}_1^0}^2$ in the above equations. The mass function $g_{AV}(x)$ is defined in Eq.(A.6). Y is the hypercharge and n is the n -tuple. We take $n = 2$ and $Y^2 = \frac{1}{4}$ for the Higgsino case (pure limit), and $n = 3$ and $Y = 0$ for the Wino case (pure limit). $T_{3u} = \frac{1}{2}$ and $T_{3d/s} = -\frac{1}{2}$, meanwhile $Q_u = \frac{2}{3}$ and $Q_{d/s} = -\frac{1}{3}$. θ_W is the weak mixing angle. The experimental values of the quark contribution to the spin of the nucleons for the light quarks, the Δq_N 's, are taken to be [81]

$$\Delta u_p = 0.842, \quad \Delta d_p = -0.427, \quad \Delta s_p = -0.085, \quad (\text{A.5a})$$

$$\Delta d_n = 0.842, \quad \Delta u_n = -0.427, \quad \Delta s_n = -0.085. \quad (\text{A.5b})$$

These values are confirmed by the HERMES collaboration [79] as well as by the COMPASS collaboration [109].

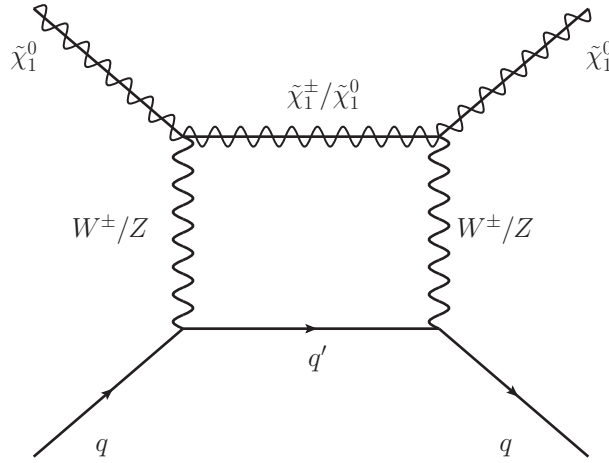


FIG. 5. W^\pm/Z box diagram for the neutralino-quark scattering process.

The mass function used in Eq.(A.3) is given as

$$g_{AV}(x) = \frac{1}{24b_x} \sqrt{x}(8 - x - x^2) \tan^{-1} \left(\frac{2b_x}{\sqrt{x}} \right) - \frac{1}{24} x(2 - (3 + x) \log(x)) \quad (\text{A.6})$$

with $b_x = \sqrt{1 - x/4}$.

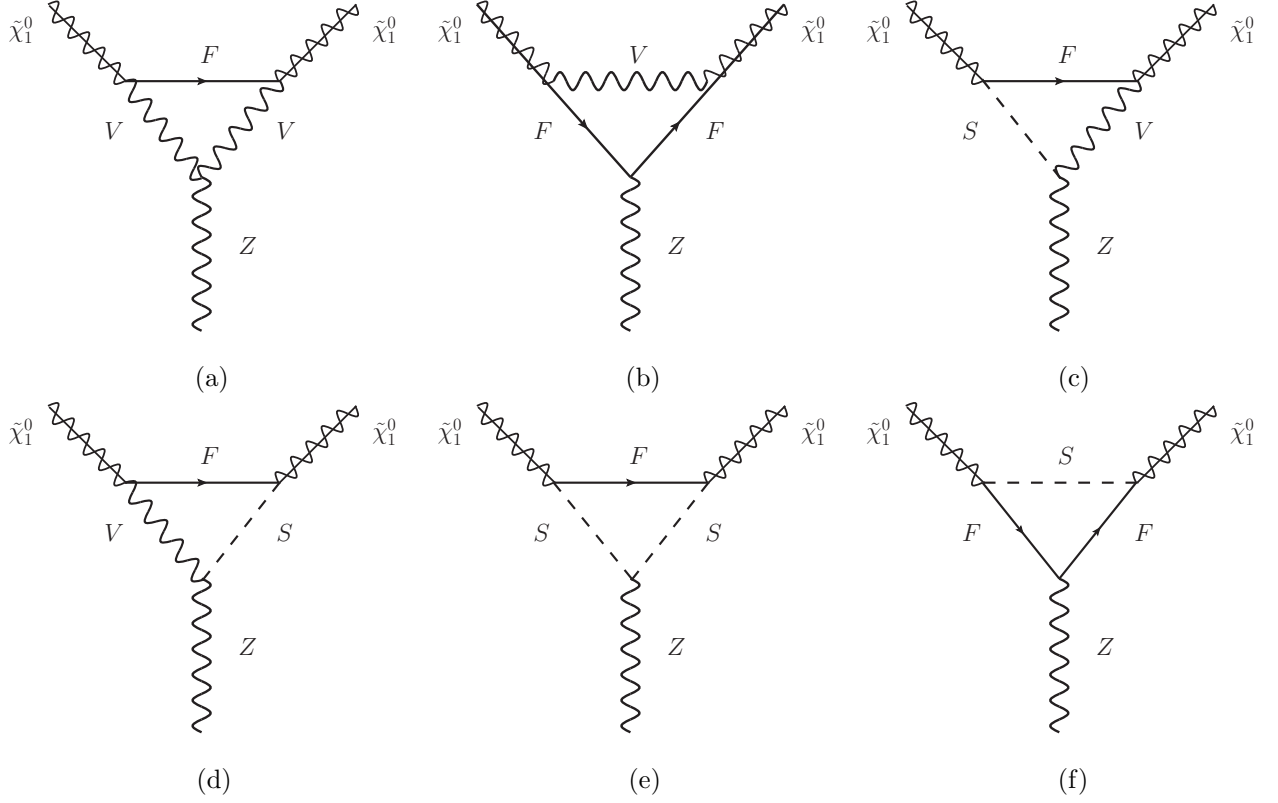


FIG. 6. Topologies for the $\tilde{\chi}_1^0 \tilde{\chi}_1^0 Z$ vertex radiative correction diagrams are shown in panels (a)-(f). Here, F represents fermions in the loop, V represents vector bosons and S represents scalar particles.

APPENDIX B: VERTEX CORRECTION EVALUATION

There are 292 loop diagrams contributing to the vertex corrections, which can be categorized into six distinct topologies as depicted in Fig.6. For simplicity, we provide the explicit expressions for the four most dominant diagrams in our evaluation. The leading diagrams are illustrated in Fig.7 and Fig.8, with their corresponding analytical expressions given in Eqs.(B.1), (B.2), (B.3), and (B.4). Contributions from the remaining diagrams are comparatively smaller and thus, their analytical expressions are omitted in this article. However, the expressions for these subdominant diagrams can be derived using the Feynman rules outlined in Ref.[66] or with the aid of **FeynArts** [88].

The mathematical equation for the Feynman diagram topology 1 in Fig.7(a) is given as:

$$i\delta\Gamma^{(1)} = \frac{i}{16\pi^2} \left\{ \gamma^\mu \mathbf{P}_L \left\{ T_{1R} T_{3L} [m_t^2 T_{2R} C_0 - 2T_{2L} C_{00} - m_{\tilde{\chi}_1^0}^2 T_{2L} (C_{22} + 2C_{12} + C_{11} + C_2 + C_1)] \right\} \right. \\ \left. + \gamma^\mu \mathbf{P}_R \left\{ T_{1L} T_{3R} [m_t^2 T_{2L} C_0 - 2T_{2R} C_{00} - m_{\tilde{\chi}_1^0}^2 T_{2R} (C_{22} + 2C_{12} + C_{11} + C_2 + C_1)] \right\} \right\}, \quad (\text{B.1})$$

where $C_i = C_i(m_{\tilde{\chi}_1^0}^2, q^2, m_{\tilde{\chi}_1^0}^2; m_{\tilde{t}^s}, m_t, m_t)$ and $C_{ij} = C_{ij}(m_{\tilde{\chi}_1^0}^2, q^2, m_{\tilde{\chi}_1^0}^2; m_{\tilde{t}^s}, m_t, m_t)$ are the Passarino-

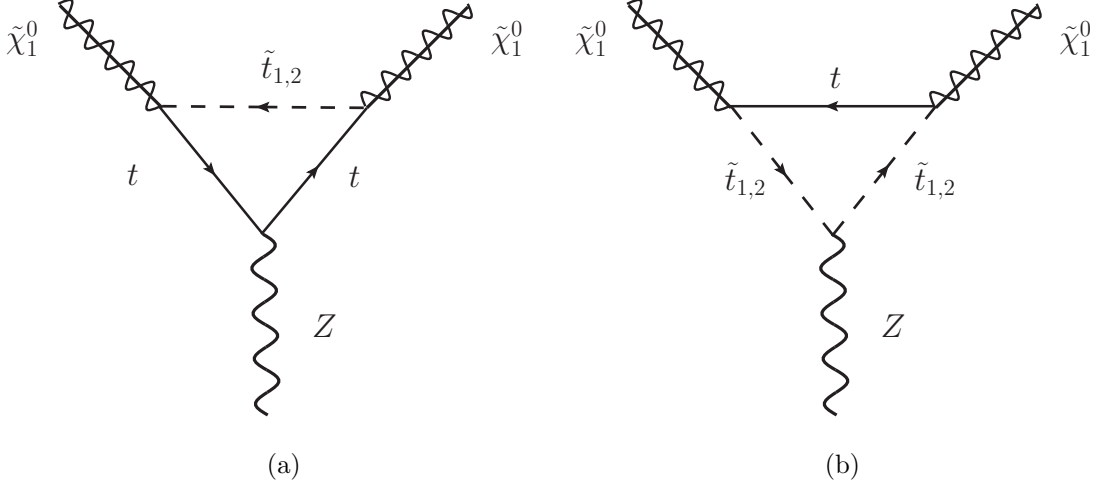


FIG. 7. Topology 1 (panel(a)) and Topology 2 (panel (b)).

Veltman functions [110]. We have followed the convention of Refs.[111, 112]. The explicit expressions for some of the relevant C functions are shown in the Appendix of Ref.[40]. Further,

$$\begin{aligned}
 T_{1L} &= \frac{g_1[4M_W s_\beta s_W \mathcal{U}_{\tilde{t}}(s, 2)N_{11} - 3c_W m_t \mathcal{U}_{\tilde{t}}(s, 1)N_{14}]}{3\sqrt{2}s_W s_\beta M_W}, \\
 T_{1R} &= -\frac{g_1[M_W s_\beta \mathcal{U}_{\tilde{t}}(s, 1)(s_W N_{11} + 3c_W N_{12}) + 3c_W m_t \mathcal{U}_{\tilde{t}}(s, 2)N_{14}]}{3\sqrt{2}s_W s_\beta M_W}, \\
 T_{2L} &= \frac{2g_1 s_W}{3}, \quad T_{2R} = \frac{g_1(1 - 4c_W^2)}{6s_W}, \\
 T_{3L} &= T_{1R}, \quad T_{3R} = T_{1L}.
 \end{aligned}$$

In the above equations (as well as the following ones), $i, j, s = 1, 2$, $s_W = \sin \theta_W$, $c_W = \cos \theta_W$, $s_\beta = \sin \beta$, and $\mathcal{U}_{\tilde{t}}(s, k)$ are the stop mixing matrix elements, where $k = 1, 2$.

Topology 2, Fig.7(b):

$$i\delta\Gamma^{(2)} = -\frac{i\xi}{16\pi^2} \left\{ \gamma^\mu \mathbf{P}_L [2S_{1R}S_{2L}C_{00}] + \gamma^\mu \mathbf{P}_R [2S_{1L}S_{2R}C_{00}] \right\}, \quad (\text{B.2})$$

where, $C_i = C_i(m_{\tilde{\chi}_1^0}^2, q^2, m_{\tilde{\chi}_1^0}^2; m_t, m_{\tilde{t}_s}, m_{\tilde{t}_s})$, and $C_{ij} = C_{ij}(m_{\tilde{\chi}_1^0}^2, q^2, m_{\tilde{\chi}_1^0}^2; m_t, m_{\tilde{t}_s}, m_{\tilde{t}_s})$. Further,

$$\begin{aligned}
 \xi &= \frac{g_1}{3s_W} [(1 - 4c_W^2)\mathcal{U}_{\tilde{t}_s}^2(s, 1) + 4s_W^2\mathcal{U}_{\tilde{t}_s}^2(s, 2)], \\
 S_{1L} &= \frac{g_1[M_W s_\beta \mathcal{U}_{\tilde{t}_s}(s, 1)\{s_W N_{11} + 3c_W N_{12}\} + 3c_W m_t \mathcal{U}_{\tilde{t}_s}(s, 2)N_{14}]}{3\sqrt{2}M_W s_\beta s_W}, \\
 S_{1R} &= \frac{g_1[-4M_W s_\beta s_W \mathcal{U}_{\tilde{t}_s}(s, 2)N_{11} + 3c_W m_t \mathcal{U}_{\tilde{t}_s}(s, 1)N_{14}]}{3\sqrt{2}M_W s_\beta s_W}, \\
 S_{2L} &= -S_{1R}, \quad S_{2R} = -S_{1L}.
 \end{aligned}$$

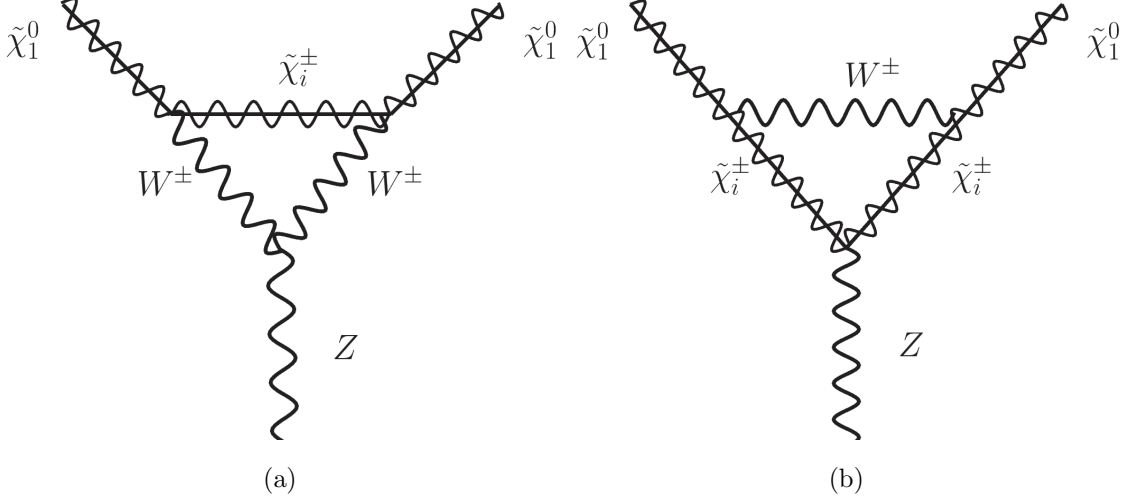


FIG. 8. Topology 3 (panel (a)) and Topology 4 (panel (b)).

Topology 3, Fig.8(a):

$$i\delta\Gamma^{(3)} = \pm \frac{ig_2c_W}{16\pi^2} \left\{ \gamma^\mu \mathbf{P}_L \left[2Q_{2L}(-2Q_{1L}C_{00} + m_{\tilde{\chi}_1^0}^2 Q_{1L}(C_2 - C_1) + m_{\tilde{\chi}_1^0} m_{\tilde{\chi}_i^\pm} Q_{1R}(2C_0 + C_2 - C_1)) \right] \right. \\ \left. + \gamma^\mu \mathbf{P}_R \left[2Q_{2R}(m_{\tilde{\chi}_1^0} m_{\tilde{\chi}_i^\pm} Q_{1L}(2C_0 + C_2 - C_1) - 2Q_{1R}C_{00} + m_{\tilde{\chi}_1^0}^2 Q_{1R}(C_2 - C_1)) \right] \right\}, \quad (\text{B.3})$$

where, $C_j = C_j(m_{\tilde{\chi}_1^0}^2, q^2, m_{\tilde{\chi}_1^0}^2; m_{\tilde{\chi}_i^\pm}, M_W, M_W)$, and $C_{jk} = C_{jk}(m_{\tilde{\chi}_1^0}^2, q^2, m_{\tilde{\chi}_1^0}^2; m_{\tilde{\chi}_i^\pm}, M_W, M_W)$. Further,

$$Q_{1L} = -g_2 \left(\pm V_{i1} N_{12} - \frac{V_{i2} N_{14}}{\sqrt{2}} \right), \quad Q_{1R} = -g_2 \left(\pm U_{i1} N_{12} + \frac{U_{i2} N_{13}}{\sqrt{2}} \right), \\ Q_{2L} = Q_{1L}, \quad Q_{2R} = Q_{1R}.$$

From Eq.(B.3) it is evident that the loop diagrams involving $(W^+, \tilde{\chi}_i^+)$ and the $(W^-, \tilde{\chi}_i^-)$ in Fig.8(a), contribute destructively and there is a partial cancellation between the positive and the negative charge diagrams. This leads to a small contribution from this diagram in the Higgsino case, as this cancellation is not exact. In the pure Higgsino limit (and the pure Wino limit), this cancellation is exact and the contribution from this diagram vanishes for both the symmetric and anti-symmetric cases of the Higgsino-like (and Wino-like) benchmarks.

Topology 4, Fig.8(b):

$$i\delta\Gamma^{(4)} = \pm \frac{i}{16\pi^2} \left\{ \gamma^\mu \mathbf{P}_L \left[F_{2L} \{ F_{1L} O_L (4C_{00} + m_{\tilde{\chi}_1^0}^2 (2C_{22} + 2(2C_{12} + C_{11}) + 6C_0 + 8C_2 + 8C_1)) \right. \right. \\ \left. \left. - 2F_{1L} O_R m_{\tilde{\chi}_i^\pm}^2 C_0 \right\} + \gamma^\mu \mathbf{P}_R \left[F_{2R} \{ -2F_{1R} O_L m_{\tilde{\chi}_i^\pm}^2 C_0 + F_{1R} O_R (4C_{00} + \right. \right. \\ \left. \left. m_{\tilde{\chi}_1^0}^2 (2C_{22} + 2(2C_{12} + C_{11}) + 6C_0 + 8C_2 + 8C_1)) \right\} \right] \right\}, \quad (\text{B.4})$$

where, $C_j = C_j(m_{\tilde{\chi}_1^0}^2, q^2, m_{\tilde{\chi}_1^\pm}^2; M_W, m_{\tilde{\chi}_i^\pm}, m_{\tilde{\chi}_i^\pm})$, and $C_{jk} = C_{jk}(m_{\tilde{\chi}_1^0}^2, q^2, m_{\tilde{\chi}_1^\pm}^2; M_W, m_{\tilde{\chi}_i^\pm}, m_{\tilde{\chi}_i^\pm})$. Further,

$$\begin{aligned}
 F_{1L} &= -g_2 \left(\pm V_{i1} N_{12} - \frac{V_{i2} N_{14}}{\sqrt{2}} \right), & F_{1R} &= -g_2 \left(\pm U_{i1} N_{12} + \frac{U_{i2} N_{13}}{\sqrt{2}} \right), \\
 F_{2L} &= F_{1L}, & F_{2R} &= F_{1R}, \\
 O_L &= \frac{g_2}{2c_W} (-2s_W^2 + 2|V_{11}|^2 + |V_{12}|^2), & O_R &= \frac{g_2}{2c_W} (-2s_W^2 + 2|U_{11}|^2 + |U_{12}|^2).
 \end{aligned}$$

Similar to the previous case, in Eq.(B.4) we see a partial cancellation between the diagrams involving $(W^+, \tilde{\chi}_i^+)$ and the $(W^-, \tilde{\chi}_i^-)$ states in Fig.8(b) resulting in a relatively diminished contribution especially in the Higgsino case. This cancellation is inexact, leading to a non-zero contribution in our case. In the pure Higgsino limit (and the pure Wino one), this is an exact cancellation and this loop diagram vanishes as well for both the symmetric and anti-symmetric cases of the Higgsino-like (and Wino-like) benchmarks.

-
- [1] G. Bertone, D. Hooper and J. Silk, *Particle dark matter: Evidence, candidates and constraints*, *Phys. Rept.* **405** (2005) 279–390, [[hep-ph/0404175](#)].
 - [2] J. Silk et al., *Particle Dark Matter: Observations, Models and Searches*. Cambridge Univ. Press, Cambridge, 2010, 10.1017/CBO9780511770739.
 - [3] G. Bertone and D. Hooper, *History of dark matter*, *Rev. Mod. Phys.* **90** (2018) 045002, [[1605.04909](#)].
 - [4] PLANCK collaboration, N. Aghanim et al., *Planck 2018 results. VI. Cosmological parameters*, *Astron. Astrophys.* **641** (2020) A6, [[1807.06209](#)]. [Erratum: *Astron. Astrophys.* 652, C4 (2021)].
 - [5] PLANCK collaboration, P. A. R. Ade et al., *Planck 2013 results. I. Overview of products and scientific results*, *Astron. Astrophys.* **571** (2014) A1, [[1303.5062](#)].
 - [6] G. Jungman, M. Kamionkowski and K. Griest, *Supersymmetric dark matter*, *Phys. Rept.* **267** (1996) 195–373, [[hep-ph/9506380](#)].
 - [7] R. Barbieri and G. F. Giudice, *Upper Bounds on Supersymmetric Particle Masses*, *Nucl. Phys.* **B306** (1988) 63–76.
 - [8] J. Ellis, K. Enqvist, D. Nanopoulos and F. Zwirner, *Observables in low-energy superstring models*, *Modern Physics Letters A* **01** (1986) 57–69, [<https://doi.org/10.1142/S0217732386000105>].
 - [9] K. L. Chan, U. Chattopadhyay and P. Nath, *Naturalness, weak scale supersymmetry and the prospect for the observation of supersymmetry at the Tevatron and at the CERN LHC*, *Phys. Rev. D* **58** (1998) 096004, [[hep-ph/9710473](#)].
 - [10] J. L. Feng, *Naturalness and the Status of Supersymmetry*, *Ann. Rev. Nucl. Part. Sci.* **63** (2013) 351–382, [[1302.6587](#)].
 - [11] G. F. Giudice, *Naturalness after LHC8*, *PoS EPS-HEP2013* (2013) 163, [[1307.7879](#)].

- [12] H. Baer, V. Barger, P. Huang, D. Mickelson, A. Mustafayev and X. Tata, *Radiative natural supersymmetry: Reconciling electroweak fine-tuning and the Higgs boson mass*, *Phys. Rev. D* **87** (2013) 115028, [1212.2655].
- [13] A. Mustafayev and X. Tata, *Supersymmetry, Naturalness, and Light Higgsinos*, *Indian J. Phys.* **88** (2014) 991–1004, [1404.1386].
- [14] ATLAS collaboration, G. Aad et al., *Search for charginos and neutralinos in final states with two boosted hadronically decaying bosons and missing transverse momentum in pp collisions at $\sqrt{s} = 13$ TeV with the ATLAS detector*, *Phys. Rev. D* **104** (2021) 112010, [2108.07586].
- [15] ATLAS collaboration, G. Aad et al., *Search for chargino-neutralino production with mass splittings near the electroweak scale in three-lepton final states in $\sqrt{s}=13$ TeV pp collisions with the ATLAS detector*, *Phys. Rev. D* **101** (2020) 072001, [1912.08479].
- [16] ATLAS collaboration, G. Aad et al., *Searches for new phenomena in events with two leptons, jets, and missing transverse momentum in 139 fb^{-1} of $\sqrt{s} = 13$ TeV pp collisions with the ATLAS detector*, *Eur. Phys. J. C* **83** (2023) 515, [2204.13072].
- [17] ATLAS collaboration, G. Aad et al., *Search for direct pair production of sleptons and charginos decaying to two leptons and neutralinos with mass splittings near the W-boson mass in $\sqrt{s} = 13$ TeV pp collisions with the ATLAS detector*, *JHEP* **06** (2023) 031, [2209.13935].
- [18] ATLAS collaboration, G. Aad et al., *Search for chargino-neutralino pair production in final states with three leptons and missing transverse momentum in $\sqrt{s} = 13$ TeV pp collisions with the ATLAS detector*, *Eur. Phys. J. C* **81** (2021) 1118, [2106.01676].
- [19] CMS collaboration, A. Tumasyan et al., *Search for electroweak production of charginos and neutralinos at $s=13\text{TeV}$ in final states containing hadronic decays of WW, WZ, or WH and missing transverse momentum*, *Phys. Lett. B* **842** (2023) 137460, [2205.09597].
- [20] CMS collaboration, A. Hayrapetyan et al., *Search for new physics in multijet events with at least one photon and large missing transverse momentum in proton-proton collisions at 13 TeV*, *JHEP* **10** (2023) 046, [2307.16216].
- [21] H. Baer, V. Barger, P. Huang, A. Mustafayev and X. Tata, *Radiative natural SUSY with a 125 GeV Higgs boson*, *Phys. Rev. Lett.* **109** (2012) 161802, [1207.3343].
- [22] H. Baer, V. Barger, P. Huang, D. Mickelson, A. Mustafayev and X. Tata, *Naturalness, Supersymmetry and Light Higgsinos: A Snowmass Whitepaper*, in *Proceedings, Community Summer Study 2013: Snowmass on the Mississippi (CSS2013): Minneapolis, MN, USA, July 29-August 6, 2013*, 2013. 1306.2926.
- [23] K. J. Bae, H. Baer, V. Barger and D. Sengupta, *Revisiting the SUSY μ problem and its solutions in the LHC era*, *Phys. Rev. D* **99** (2019) 115027, [1902.10748].
- [24] H. Baer, V. Barger and D. Mickelson, *Direct and indirect detection of higgsino-like WIMPs: concluding the story of electroweak naturalness*, *Phys. Lett. B* **726** (2013) 330–336, [1303.3816].
- [25] M. Chakraborti, U. Chattopadhyay and S. Poddar, *How light a higgsino or a wino dark matter can become in a compressed scenario of MSSM*, *JHEP* **09** (2017) 064, [1702.03954].

- [26] C. Dessert, J. W. Foster, Y. Park, B. R. Safdi and W. L. Xu, *Higgsino Dark Matter Confronts 14 Years of Fermi γ -Ray Data*, *Phys. Rev. Lett.* **130** (May, 2023) 201001.
- [27] S. P. Martin, *The curtain lowers on directly detectable higgsino dark matter*, 2412.08958.
- [28] LZ collaboration, J. Aalbers et al., *First Dark Matter Search Results from the LUX-ZEPLIN (LZ) Experiment*, *Phys. Rev. Lett.* **131** (2023) 041002, [2207.03764].
- [29] XENON collaboration, E. Aprile et al., *First Dark Matter Search with Nuclear Recoils from the XENONnT Experiment*, *Phys. Rev. Lett.* **131** (2023) 041003, [2303.14729].
- [30] PANDAX-II collaboration, Q. Wang et al., *Results of dark matter search using the full PandaX-II exposure*, *Chin. Phys. C* **44** (2020) 125001, [2007.15469].
- [31] PICO COLLABORATION collaboration, C. Amole, M. Ardid, I. J. Arnquist, D. M. Asner, D. Baxter, E. Behnke et al., *Dark matter search results from the complete exposure of the PICO-60 C₃F₈ bubble chamber*, *Phys. Rev. D* **100** (Jul, 2019) 022001.
- [32] MAGIC, FERMI-LAT collaboration, M. L. Ahnen et al., *Limits to Dark Matter Annihilation Cross-Section from a Combined Analysis of MAGIC and Fermi-LAT Observations of Dwarf Satellite Galaxies*, *JCAP* **02** (2016) 039, [1601.06590].
- [33] FERMI-LAT, DES collaboration, A. Albert et al., *Searching for Dark Matter Annihilation in Recently Discovered Milky Way Satellites with Fermi-LAT*, *Astrophys. J.* **834** (2017) 110, [1611.03184].
- [34] THE FERMI-LAT COLLABORATION collaboration, M. Ackermann, A. Albert, B. Anderson, W. B. Atwood, L. Baldini, G. Barbiellini et al., *Searching for dark matter annihilation from milky way dwarf spheroidal galaxies with six years of fermi large area telescope data*, *Phys. Rev. Lett.* **115** (Nov, 2015) 231301.
- [35] U. Chattopadhyay, D. Das, S. Poddar, R. Puri and A. K. Saha, *Implications of Sgr A* on the γ -rays searches of Bino dark matter with $(g-2)_\mu$* , *JCAP* **01** (2025) 121, [2407.14603].
- [36] M. Drees, M. M. Nojiri, D. P. Roy and Y. Yamada, *Light Higgsino dark matter*, *Phys. Rev. D* **56** (1997) 276–290, [hep-ph/9701219]. [Erratum: Phys.Rev.D 64, 039901 (2001)].
- [37] J. Hisano, S. Matsumoto, M. M. Nojiri and O. Saito, *Direct detection of the Wino and Higgsino-like neutralino dark matters at one-loop level*, *Phys. Rev. D* **71** (2005) 015007, [hep-ph/0407168].
- [38] J. Hisano, K. Ishiwata, N. Nagata and T. Takesako, *Direct Detection of Electroweak-Interacting Dark Matter*, *JHEP* **07** (2011) 005, [1104.0228].
- [39] J. Hisano, K. Ishiwata and N. Nagata, *Direct Search of Dark Matter in High-Scale Supersymmetry*, *Phys. Rev. D* **87** (2013) 035020, [1210.5985].
- [40] S. Bisal, A. Chatterjee, D. Das and S. A. Pasha, *Radiative corrections to aid the direct detection of the Higgsino-like neutralino dark matter: Spin-independent interactions*, *Phys. Rev. D* **110** (2024) 023043, [2311.09937].
- [41] S. Bisal, A. Chatterjee, D. Das and S. A. Pasha, *Electroweak renormalization of neutralino-Higgs interactions at one-loop and its impacts on spin-independent direct detection of Wino-like dark matter*, 2410.18206.
- [42] N. Baro, F. Boudjema and A. Semenov, *Full one-loop corrections to the relic density in the MSSM: A Few*

- examples, *Phys. Lett. B* **660** (2008) 550–560, [0710.1821].
- [43] N. Baro, F. Boudjema, G. Chalons and S. Hao, *Relic density at one-loop with gauge boson pair production*, *Phys. Rev. D* **81** (2010) 015005, [0910.3293].
- [44] A. Chatterjee, M. Drees and S. Kulkarni, *Radiative Corrections to the Neutralino Dark Matter Relic Density - an Effective Coupling Approach*, *Phys. Rev. D* **86** (2012) 105025, [1209.2328].
- [45] J. Harz, B. Herrmann, M. Klasen, K. Kovařík and M. Meinecke, *SUSY-QCD corrections to stop annihilation into electroweak final states including Coulomb enhancement effects*, *Phys. Rev. D* **91** (2015) 034012, [1410.8063].
- [46] J. Harz, B. Herrmann, M. Klasen and K. Kovarik, *One-loop corrections to neutralino-stop coannihilation revisited*, *Phys. Rev. D* **91** (2015) 034028, [1409.2898].
- [47] M. Klasen, K. Kovarik and P. Steppeler, *SUSY-QCD corrections for direct detection of neutralino dark matter and correlations with relic density*, *Phys. Rev. D* **94** (2016) 095002, [1607.06396].
- [48] J. Harz, B. Herrmann, M. Klasen, K. Kovařík and L. P. Wiggering, *Precision predictions for dark matter with DM@NLO in the MSSM*, 2312.17206.
- [49] S. Bisal, A. Chatterjee, D. Das and S. A. Pasha, *Confronting electroweak MSSM through one-loop renormalized neutralino-Higgs interactions for dark matter direct detection and muon ($g-2$)*, 2311.09938.
- [50] T. Fritzsche and W. Hollik, *Complete one loop corrections to the mass spectrum of charginos and neutralinos in the MSSM*, *Eur. Phys. J. C* **24** (2002) 619–629, [hep-ph/0203159].
- [51] N. Baro and F. Boudjema, *Automatized full one-loop renormalization of the mssm. ii. the chargino-neutralino sector, the sfermion sector, and some applications*, *Phys. Rev. D* **80** (Oct, 2009) 076010.
- [52] A. Chatterjee, M. Drees, S. Kulkarni and Q. Xu, *On the On-Shell Renormalization of the Chargino and Neutralino Masses in the MSSM*, *Phys. Rev. D* **85** (2012) 075013, [1107.5218].
- [53] G. Belanger, F. Boudjema, A. Pukhov and A. Semenov, *micrOMEGAs: A Tool for dark matter studies*, *Nuovo Cim. C* **033N2** (2010) 111–116, [1005.4133].
- [54] G. Belanger, F. Boudjema, A. Pukhov and A. Semenov, *micrOMEGAs.3: A program for calculating dark matter observables*, *Comput. Phys. Commun.* **185** (2014) 960–985, [1305.0237].
- [55] J. Hisano, K. Ishiwata and N. Nagata, *A complete calculation for direct detection of Wino dark matter*, *Phys. Lett. B* **690** (2010) 311–315, [1004.4090].
- [56] L. Randall and R. Sundrum, *Out of this world supersymmetry breaking*, *Nucl. Phys. B* **557** (1999) 79–118, [hep-th/9810155].
- [57] G. F. Giudice, M. A. Luty, H. Murayama and R. Rattazzi, *Gaugino mass without singlets*, *JHEP* **12** (1998) 027, [hep-ph/9810442].
- [58] J. Hisano, S. Matsumoto, M. Nagai, O. Saito and M. Senami, *Non-perturbative effect on thermal relic abundance of dark matter*, *Phys. Lett. B* **646** (2007) 34–38, [hep-ph/0610249].
- [59] M. Beneke, C. Hellmann and P. Ruiz-Femenia, *Heavy neutralino relic abundance with Sommerfeld enhancements - a study of pMSSM scenarios*, *JHEP* **03** (2015) 162, [1411.6930].

- [60] J. Hisano, S. Matsumoto, M. M. Nojiri and O. Saito, *Non-perturbative effect on dark matter annihilation and gamma ray signature from galactic center*, *Phys. Rev. D* **71** (2005) 063528, [[hep-ph/0412403](#)].
- [61] S. Mohanty, S. Rao and D. P. Roy, *Relic density and PAMELA events in a heavy wino dark matter model with Sommerfeld effect*, *Int. J. Mod. Phys. A* **27** (2012) 1250025, [[1009.5058](#)].
- [62] M. Beneke, R. Szafron and K. Urban, *Wino potential and Sommerfeld effect at NLO*, *Phys. Lett. B* **800** (2020) 135112, [[1909.04584](#)].
- [63] M. Chakraborti, U. Chattopadhyay, A. Choudhury, A. Datta and S. Poddar, *Reduced LHC constraints for higgsino-like heavier electroweakinos*, *JHEP* **11** (2015) 050, [[1507.01395](#)].
- [64] L. Aparicio, M. Cicoli, B. Dutta, F. Muia and F. Quevedo, *Light Higgsino Dark Matter from Non-thermal Cosmology*, *JHEP* **11** (2016) 038, [[1607.00004](#)].
- [65] K. J. Bae, H. Baer and E. J. Chun, *Mixed axion/neutralino dark matter in the SUSY DFSZ axion model*, *JCAP* **12** (2013) 028, [[1309.5365](#)].
- [66] M. Drees, R. Godbole and P. Roy, *Theory and phenomenology of sparticles: An account of four-dimensional N=1 supersymmetry in high energy physics*. 2004.
- [67] V. Barger, M. S. Berger and P. Ohmann, *Supersymmetric particle spectrum*, *Phys. Rev. D* **49** (May, 1994) 4908–4930.
- [68] M. M. El Kheishen, A. A. Shafik and A. A. Aboshousha, *Analytic formulas for the neutralino masses and the neutralino mixing matrix*, *Phys. Rev. D* **45** (Jun, 1992) 4345–4348.
- [69] S. Y. Choi, J. Kalinowski, G. A. Moortgat-Pick and P. M. Zerwas, *Analysis of the neutralino system in supersymmetric theories*, *Eur. Phys. J. C* **22** (2001) 563–579, [[hep-ph/0108117](#)]. [Addendum: *Eur.Phys.J.C* **23**, 769–772 (2002)].
- [70] G. F. Giudice and A. Pomarol, *Mass degeneracy of the Higgsinos*, *Phys. Lett. B* **372** (1996) 253–258, [[hep-ph/9512337](#)].
- [71] G. D. Kribs, A. Martin and T. S. Roy, *Supersymmetry with a Chargino NLSP and Gravitino LSP*, *JHEP* **01** (2009) 023, [[0807.4936](#)].
- [72] Z. Han, G. D. Kribs, A. Martin and A. Menon, *Hunting quasidegenerate Higgsinos*, *Phys. Rev.* **D89** (2014) 075007, [[1401.1235](#)].
- [73] D. Barducci, A. Belyaev, A. K. M. Bharucha, W. Porod and V. Sanz, *Uncovering Natural Supersymmetry via the interplay between the LHC and Direct Dark Matter Detection*, *JHEP* **07** (2015) 066, [[1504.02472](#)].
- [74] A. Chatterjee, J. Dutta and S. K. Rai, *Natural SUSY at LHC with Right-Sneutrino LSP*, *JHEP* **06** (2018) 042, [[1710.10617](#)].
- [75] M. W. Goodman and E. Witten, *Detectability of Certain Dark Matter Candidates*, *Phys. Rev. D* **31** (1985) 3059.
- [76] K. Griest, *Calculations of rates for direct detection of neutralino dark matter*, *Phys. Rev. Lett.* **61** (Aug, 1988) 666–669.
- [77] M. Drees and M. M. Nojiri, *Neutralino-nucleon scattering reexamined*, *Phys. Rev. D* **48** (Oct, 1993)

3483–3501.

- [78] K. Griest, *Cross-Sections, Relic Abundance and Detection Rates for Neutralino Dark Matter*, *Phys. Rev. D* **38** (1988) 2357. [Erratum: *Phys.Rev.D* 39, 3802 (1989)].
- [79] HERMES collaboration, A. Airapetian et al., *Precise determination of the spin structure function $g(1)$ of the proton, deuteron and neutron*, *Phys. Rev. D* **75** (2007) 012007, [[hep-ex/0609039](#)].
- [80] J. Engel, S. Pittel and P. Vogel, *Nuclear physics of dark matter detection*, *Int. J. Mod. Phys. E* **1** (1992) 1–37.
- [81] G. Belanger, F. Boudjema, A. Pukhov and A. Semenov, *Dark matter direct detection rate in a generic model with micrOMEGAs 2.2*, *Comput. Phys. Commun.* **180** (2009) 747–767, [[0803.2360](#)].
- [82] V. A. Bednyakov and F. Simkovic, *Nuclear spin structure in dark matter search: The Zero momentum transfer limit*, *Phys. Part. Nucl.* **36** (2005) 131–152, [[hep-ph/0406218](#)].
- [83] M. T. Ressel, M. B. Aufderheide, S. D. Bloom, K. Griest, G. J. Mathews and D. A. Resler, *Nuclear shell model calculations of neutralino - nucleus cross-sections for Si-29 and Ge-73*, *Phys. Rev. D* **48** (1993) 5519–5535, [[hep-ph/9307228](#)].
- [84] H. E. Haber and G. L. Kane, *The Search for Supersymmetry: Probing Physics Beyond the Standard Model*, *Phys. Rept.* **117** (1985) 75–263.
- [85] T. Fritzsche, T. Hahn, S. Heinemeyer, F. von der Pahlen, H. Rzehak and C. Schappacher, *The Implementation of the Renormalized Complex MSSM in FeynArts and FormCalc*, *Comput. Phys. Commun.* **185** (2014) 1529–1545, [[1309.1692](#)].
- [86] T. Hahn, *Generating Feynman diagrams and amplitudes with FeynArts 3*, *Comput. Phys. Commun.* **140** (2001) 418–431, [[hep-ph/0012260](#)].
- [87] J. Küblbeck, M. Böhm and A. Denner, *Feyn arts — computer-algebraic generation of feynman graphs and amplitudes*, *Computer Physics Communications* **60** (1990) 165–180.
- [88] T. Hahn and C. Schappacher, *The Implementation of the minimal supersymmetric standard model in FeynArts and FormCalc*, *Comput. Phys. Commun.* **143** (2002) 54–68, [[hep-ph/0105349](#)].
- [89] Hahn, T. and Perez-Victoria, M., *Automatized one loop calculations in four-dimensions and D-dimensions*, *Comput. Phys. Commun.* **118** (1999) 153–165, [[hep-ph/9807565](#)].
- [90] F. Staub and W. Porod, *Improved predictions for intermediate and heavy Supersymmetry in the MSSM and beyond*, *Eur. Phys. J. C* **77** (2017) 338, [[1703.03267](#)].
- [91] F. Staub, *SARAH 4 : A tool for (not only SUSY) model builders*, *Comput. Phys. Commun.* **185** (2014) 1773–1790, [[1309.7223](#)].
- [92] F. Staub, *Exploring new models in all detail with SARAH*, *Adv. High Energy Phys.* **2015** (2015) 840780, [[1503.04200](#)].
- [93] W. Porod, *SPheno, a program for calculating supersymmetric spectra, SUSY particle decays and SUSY particle production at $e^+ e^-$ colliders*, *Comput. Phys. Commun.* **153** (2003) 275–315, [[hep-ph/0301101](#)].
- [94] G. Belanger, F. Boudjema, A. Pukhov and A. Semenov, *MicrOMEGAs 2.0: A Program to calculate the relic density of dark matter in a generic model*, *Comput. Phys. Commun.* **176** (2007) 367–382, [[hep-ph/0607059](#)].

- [95] G. Alguero, J. Heisig, C. Khosa, S. Kraml, S. Kulkarni, A. Lessa et al., *Constraining new physics with SModelS version 2*, 2112.00769.
- [96] J. Heisig, S. Kraml and A. Lessa, *Constraining new physics with searches for long-lived particles: Implementation into SModelS*, 1808.05229.
- [97] J. Dutta, S. Kraml, A. Lessa and W. Waltenberger, *SModelS extension with the CMS supersymmetry search results from Run 2*, *LHEP* **1** (2018) 5–12, [1803.02204].
- [98] F. Ambrogi, S. Kraml, S. Kulkarni, U. Laa, A. Lessa, V. Magerl et al., *SModelS v1.1 user manual*, 1701.06586.
- [99] F. Ambrogi et al., *SModelS v1.2: long-lived particles, combination of signal regions, and other novelties*, 1811.10624.
- [100] T. Sjöstrand, S. Ask, J. R. Christiansen, R. Corke, N. Desai, P. Ilten et al., *An Introduction to PYTHIA 8.2*, *Comput. Phys. Commun.* **191** (2015) 159–177, [1410.3012].
- [101] T. Sjostrand, S. Mrenna and P. Z. Skands, *PYTHIA 6.4 Physics and Manual*, *JHEP* **0605** (2006) 026, [hep-ph/0603175].
- [102] W. Beenakker, R. Hopker, M. Spira and P. Zerwas, *Squark and gluino production at hadron colliders*, *Nucl.Phys.* **B492** (1997) 51–103, [hep-ph/9610490].
- [103] A. Buckley, *PySLHA: a Pythonic interface to SUSY Les Houches Accord data*, 1305.4194.
- [104] LZ COLLABORATION collaboration, J. Aalbers et al., *Dark Matter Search Results from 4.2 Tonne-Years of Exposure of the LUX-ZEPLIN (LZ) Experiment*, 2410.17036.
- [105] PANDA-X, PANDAX collaboration, A. Abdukerim et al., *PandaX-xT—A deep underground multi-ten-tonne liquid xenon observatory*, *Sci. China Phys. Mech. Astron.* **68** (2025) 221011, [2402.03596].
- [106] XENON collaboration, E. Aprile et al., *Projected WIMP sensitivity of the XENONnT dark matter experiment*, *JCAP* **11** (2020) 031, [2007.08796].
- [107] DARWIN collaboration, J. Aalbers et al., *DARWIN: towards the ultimate dark matter detector*, *JCAP* **11** (2016) 017, [1606.07001].
- [108] DARKSIDE-20K collaboration, C. E. Aalseth et al., *DarkSide-20k: A 20 tonne two-phase LAr TPC for direct dark matter detection at LNGS*, *Eur. Phys. J. Plus* **133** (2018) 131, [1707.08145].
- [109] COMPASS collaboration, E. S. Ageev et al., *Spin asymmetry $A1(d)$ and the spin-dependent structure function $g1(d)$ of the deuteron at low values of x and Q^{*2}* , *Phys. Lett. B* **647** (2007) 330–340, [hep-ex/0701014].
- [110] G. Passarino and M. Veltman, *One-loop corrections for $e+e-$ annihilation into $\mu^+\mu^-$ in the weinberg model*, *Nuclear Physics B* **160** (1979) 151–207.
- [111] H. H. Patel, *Package-X: A Mathematica package for the analytic calculation of one-loop integrals*, *Comput. Phys. Commun.* **197** (2015) 276–290, [1503.01469].
- [112] G. van Oldenborgh, *Ff — a package to evaluate one-loop feynman diagrams*, *Computer Physics Communications* **66** (1991) 1–15.